Master's thesis

NTNU
Norwegian University of Science and Technology
Faculty of Information Technology and Electrical Engineering
Department of Electronic Systems

Håvard M. Årdal

Surface Roughness in Metallic Thin Films and its Effects on the Magnetic Properties of Permalloy Thin Films

Master's thesis in Nanotechnology
Supervisor: Erik Folven
Co-supervisor: Anders Strømberg and Jakob Vinje
June 2022

NTNU
Kunnskap for en bedre verden

Håvard M. Årdal

Surface Roughness in Metallic Thin Films and its Effects on the Magnetic Properties of Permalloy Thin Films

Master's thesis in Nanotechnology
Supervisor: Erik Folven
Co-supervisor: Anders Strømberg and Jakob Vinje
June 2022

Norwegian University of Science and Technology
Faculty of Information Technology and Electrical Engineering
Department of Electronic Systems

NTNU
Norwegian University of
Science and Technology

Abstract

Ferromagnetic permalloy (Py) thin films are extensively used in various applications, such as magnetic data storage and artificial spin ice systems. As the dimensions of the devices get smaller, the influence of surface roughness on the magnetic properties of the Py thin films gets more prominent. For artificial spin ices, local magnetic field devices have introduced new possibilities. However, challenges emerge since the nanomagnets in the artificial spin-ice are deposited onto a rough metallic substrate. Therefore, the primary purpose of this thesis was to thoroughly investigate the surface properties of the metallic thin film candidates for local field devices and use this to explain how the magnetic behavior of Py thin films is altered for different substrates.

Metallic thin films of Ti/Au and Ti/Cu/Al multilayers were prepared using electron beam evaporation. Substrates with rms roughness ranging from 0.1 nm to 2.3 nm were fabricated by varying the thickness of the Cu layer. The surfaces were characterized using an atomic force microscope, and the most crucial surface characteristics were analyzed. Circular Py thin films with a thickness of 20 nm and an Al protection layer of 2.5 nm were deposited on top of the Ti/Cu/Al layers with a fabrication process using photolithography. Scanning electron microscope images revealed that evaporation of Au was prone to spitting, making it a poor choice for local magnetic field devices.

A vibrating-sample magnetometer was used to obtain magnetization hysteresis curves from the Py discs. The coercive field of 20 nm Py films was strongly influenced by the surface structure of the substrate. Analysis of the hysteresis shapes concluded that domain wall pinning is the most prominent mechanism behind the coercive field. The domain wall pinning was more prominent when the substrate rms roughness increased. However, a deviation from this trend suggested that a more negative excess kurtosis, meaning less spiky grains, lowers the pinning energy barriers and thus also the coercive field. The saturation magnetization was found to decrease for increasing rms roughness and substrate surface area, most likely because of increased oxidation of Py.

Sammendrag

Ferromagnetisk permalloy (Py) tynnfilmer ser omfattende bruk i en rekke applikasjoner, som for eksempel i magnetisk datalagring og kunstig spinn-is systemer. Etter hvert som dimensjonene på enhetene blir mindre, blir også påvirkningen fra overflateruhet på de magnetiske egenskapene til Py tynnfilmer mer fremtredende. For kunstig spinn-is har introduksjonen av magnetiske felt indusert av metallstriper introdusert nye muligheter. Men det dukker opp utfordringer siden nanomagnetene i den kunstige spinn-isen da skal deponeres på en ru metallisk overflate. Derfor var hovedmålet med dette arbeidet å gjøre en grundig undersøkelse av overflateegenskapene til de metalliske tynnfilmene som er kandidater til magnetisk felt-induserende metallstriper, og bruke det til å forklare endringer i den magnetiske oppførselen til Py tynnfilmer deponert på ulike substrater.

Metalliske tynnfilmer bestående av Ti/Au og Ti/Cu/Al ble forberedt ved å bruke en elektronstråle evaporator. Substrater med varierende rms fra 0.1 nm til 2.3 nm ble fabrikert ved å variere tykkelsen til Cu. Overflatene ble karakterisert ved å bruke et atomkraftmikroskop og de karakteristiske egenskapene ble analysert. Sirkulære tynnfilmer av Py med en tykkelse på 20 nm og et Al beskyttelseslag på 2.5 nm ble så deponert oppå lagene med Ti/Cu/Al ved å ta i bruk fabrikkeringsprosessen fotolitografi. Bilder tatt med sveipelektronmikroskop viste at tynnfilmer med Au var utsatt for partikkelavsetting og er derfor et dårlig valg for felt-induserende metallstriper.

Et vibrerende prøvemagnometer ble brukt til å samle inn hysteresekurver fra magnetiske Py-disker. Det koersive feltet til 20 nm Py tynnfilmer ble sterkt påvirket av overflatestrukturen til substratet. Analyser av hystereseformen konkluderte at festing av domenevegger var den mest fremtredende mekanismen bak det koersive feltet. Festing av domenevegger var mer fremtredende for økende overflateruhet på substratene. Men et avvik fra denne trenden viser at en høyere overflødig utflating, som betyr mindre piggete korn, gir en lavere energibarriære for festing av domenevegger og dermed også et lavere koersivt felt. Satureringsmagnetiseringen minsket når rms økte, mest sannsynlig på grunn av økt oksidasjon av Py.

Preface

The following master's thesis has been submitted as a fulfilment of the requirements for the degree of Master of Science from the Norwegian University of Science and Technology (NTNU). The thesis is the final part of a degree in the Nanotechnology study programme, with specialisation in nanoelectronics. The work presented herein was conducted during the spring of 2022 at the Department of Electronic Systems (IES), under the guidance of Associate Professor Erik Folven at IES, and co-supervised by postdoc Jakob Vinje and Ph.D candidate Anders Strømberg.

Acknowledgements

There are many people I am grateful for at the end of this five-year-long journey in Trondheim, and I wish to use the opportunity to thank some of them.

First of all, I want to thank my three incredible supervisors for sharing your wisdom and for your support. Our meetings have been filled with exciting discussions and laughter, making it a great start to every week. Thank you, Erik Folven, for letting me perform this project and for being a genuinely nice person. Thank you, Anders Strømberg; your feedback and insight have been of much help. And last but not least, to Jakob Vinje for always being available when something goes wrong at Nanolab. Your experience and knowledge have been of great help!

The Research Council of Norway is acknowledged for the support to the Norwegian Micro- and Nano-Fabrication Facility, NorFab, project number 295864. I would also like to thank my classmate Jonas Lyng-Jørgensen for the help with the VSM measurements.

A big thanks to all my friends in the fantastic student association, Timini. Also, to Båtgutta for being amazing friends and for all the memories we have created together.

A special thanks to my parents for igniting a spark of interest in the field of mathematics, science, and technology, and to my brothers for keeping that flame alive through sparring and discussions over the years. I am very grateful for being blessed with such a lovely family. Finally, thank you, Nina, for being the most wonderful person I have ever met and making me a better version of myself.

Trondheim, June 13, 2022

Håvard M. Årdal

Contents

Chapter 1

Introduction

1.1 Motivation

Over half a century ago, in 1965, Gordon Moore predicted an accelerating change in semiconductor manufacturing which in 1975 was revised to what we know as Moore's law. In short, this is the prediction of a doubling in the number of transistors in integrated circuits every two years [1, 2]. Since then, the world has seen remarkable progress in information technology, driven by miniaturization and denser packing of the transistors. The transistor technology has moved from planar 2D structures to more advanced 3D transistor structures, constantly trying to keep up with Moore's law. However, the research community expects that beyond CMOS technology is needed to replace CMOS in some computing and information processing applications for more energy-efficient performance [3]. Increased demand for more sustainable solutions has led to an increased interest in the field of spintronics, aiming to utilize the magnetic properties of the electron.

Magnetic materials are already heavily used in successful applications, with the most prominent example being magnetic data storage in hard disk drive devices [4]. Magnetic memory devices has the advantage of being non-volatile, meaning that the magnets are capable of maintaining their magnetic state even without a power source. New and exciting research topics that utilize the magnetic spin properties of the electron spin keep emerging, one of which being artificial spin ice (ASI). Artificial spin ice is a ferromagnetic metamaterial using nanoscaled magnets as its building blocks. Each nanomagnet are capable of orienting its magnetic moment along one axis, thus having two possible states. The nanomagnets are strategically arranged on lattice sites, contributing as a small part of a larger system. The complex behavior and collective dynamics of ASIs open a wide range of applications, such as reservoir computation [5], data storage [6], and logic operations [7, 8].

As magneto-electronic technologies reduce the size of the structures, surface effects are of higher importance. One of the intriguing subjects in thin film magnetism is the effect of

surface roughness on the magnetic properties of magnetic thin films. The influence of substrate roughness has become a topic of interest for ASI structures as local magnetic field devices (striplines) were introduced. In the ongoing research on ASI for computational systems, it is interesting to see how artificial spin ice reacts to input signals, for example, in the form of alternating external magnetic fields [9]. It was proposed that local magnetic fields can be induced by controlling the current through a metallic stripline with nanomagnets fabricated directly on top of the metal. However, the surface roughness of these striplines is expected to influence the magnetic properties of the nanomagnets. Therefore, this thesis will thoroughly investigate the surface properties of possible stripline candidates and investigate and try to explain the influence of these surface properties on fabricated magnetic permalloy thin films.

Outline

The fundamentals of magnetism, ferromagnetic materials, and techniques for fabrication and characterization of nanostructures will be presented in Chapter 2, giving the reader the theoretical background needed to interpret the results. The tools, methods, and procedures that have been employed to reliable fabricate and characterize the samples are provided in Chapter 3. The methods are explained in detail, making the procedures reproducible for others. Chapter 4 will be devoted to presenting the results and providing a detailed discussion of their relevance and validity. Lastly, a conclusion and suggestions for further work will be given in Chapter 5.

Chapter 2

Background

This chapter will create the theoretical foundation to interpret and discuss the results presented later in this project. The first section will essentially provide an understanding of the subject of magnetism. Presented here are the theory and models needed to understand the behavior and characteristics of ferromagnetic materials. The second section is devoted to the art of nanofabrication, describing relevant instruments and commonly used processes. The final section will cover characterization tools that will assist the interpretation of the final results of this thesis.

2.1 Magnetism

The term magnetism is used when describing physical phenomena related to the motion of charge, magnetic materials, and the fields they generate. Magnetism is closely related to electricity, and they are, in reality, two manifestations of the same force, electromagnetism. Therefore, electric currents will generate a magnetic field and vice versa. For example, electric charges running through a wire will generate magnetic fields around the wire. Similarly, spinning magnets around a wire will induce an electric current inside the wire. These principles are utilized in everyday objects such as induction ovens. The close relation between magnetism and electricity can be expressed in a set of partial differential equations called Maxwell's equations.

The approach to describe magnetism through circular currents is called the *Amperian approach*. Another way of describing magnetism, which is highly relevant when describing magnetic materials, is to use the concept of magnetic dipoles. This is called the *Colombian approach* [10]. Magnetic poles or charges are characterized by the fact that equal poles repel each other while opposite poles attract each other, similar to electric charges. However, unlike electric charges, the magnetic fields do not allow any *sources* or *drains* but only exist in circulating fields. The non-existing sources and drains are expressed in

one of Maxwell's equations as

$$\boldsymbol{\nabla} \cdot \boldsymbol{B} = 0, \tag{2.1}$$

where $\boldsymbol{B}$ is the magnetic field.

2.1.1 The Magnetic Moment of Atoms

Knowing that magnetic poles always have to appear in pairs of opposite charges, we can introduce the magnetic dipole moment, or the magnetic moment, μ. The magnetic moment in atoms descends from its elemental particles. All atoms have a nucleus with protons and neutrons, and electrons surrounding the nucleus. The magnetic moment caused by the nucleus is much smaller than for the electrons and is therefore often neglected [11].

There are two main contributors to this magnetic moment in atoms from their electrons, spin angular moment and orbital angular moment. Electron spin is an intrinsic property present for all electrons, and each electron can either be in the spin-up or spin-down state. The orbital angular momentum is generated by electrons surrounding the nucleus, as they are creating a current loop. As we already know, this results in the creation of a magnetic field. If we add the contribution of both the spin and the angular momentum, the total magnetic moment of the electron can be written as

$$\mu_J = -g_j \frac{e}{2m_\mathrm{e}} \boldsymbol{J}, \tag{2.2}$$

where e is the elementary charge, m_e is the mass of an electron, $\boldsymbol{J}$ is the total angular momentum, and g_j is the Landé g-factor [12].

In most atoms, the contributions to the total magnetic moment from the electrons cancel out, resulting in a net-zero magnetic moment for the atom ($\boldsymbol{J} = 0$). Materials with no built-in magnetic moment, for example, noble gasses, are called diamagnets. However, some atoms contain unpaired electrons due to partially filled outer electron shells resulting in a net nonzero total angular momentum. These unpaired electrons constitute the origin of the material's magnetic properties [13].

2.1.2 Magnetic Fields, Magnetization, and Susceptibility

If we were to look at magnetism in free space (vacuum), we would find that there is no magnetization simply because there are no atoms. However, the magnetic field can still be described by the vector fields $\boldsymbol{B}$ and $\boldsymbol{H}$. In free space, they are related through the equation

$$\boldsymbol{B} = \mu_0 \boldsymbol{H}, \tag{2.3}$$

where $\mu_0 = 1.25663706212(19) \times 10^{-6}$ H/m is the permeability of free space. Both of these fields are today commonly referred to as the *magnetic field* and are distinguished by their letter (B or H) [12].

In a magnetic solid we will also have contributions to the magnetic field $\boldsymbol{B}$ from the magnetic moments inside the material. This contribution is called the magnetization, $\boldsymbol{M}$, of the material and is the macroscopic average of the magnet's intrinsic moments. It relates to $\boldsymbol{B}$ through the equation

$$\boldsymbol{B} = \mu_0 \left(\boldsymbol{H} + \boldsymbol{M} \right). \tag{2.4}$$

Magnetic materials are often classified by how their magnetization responds to an external field, $\boldsymbol{H}$, in terms of $\boldsymbol{M}$. This property vary from material to material, and is therefore ex. Therefore, we introduce the *susceptibility* defined by the equation

$$\chi \boldsymbol{H} = \boldsymbol{M}. \tag{2.5}$$

2.1.3 Classification of Magnetic Materials

Different materials will have different ordering of their magnetic moments and responses to external fields, resulting in different behavior and characteristics. Figure 2.1 illustrates four different magnetic classes schematically in the absence of external magnetic fields. Materials with random ordering of magnetic moments are called paramagnets. In comparison to diamagnets, paramagnets also have net-zero total magnetization. However, the magnetic moments in a paramagnet will align with any applied magnetic fields ($\chi > 0$). In contradiction, diamagnetic materials will set up a weak (but nonzero) magnetic field in the opposing direction of the external field ($\chi < 0$) [13].

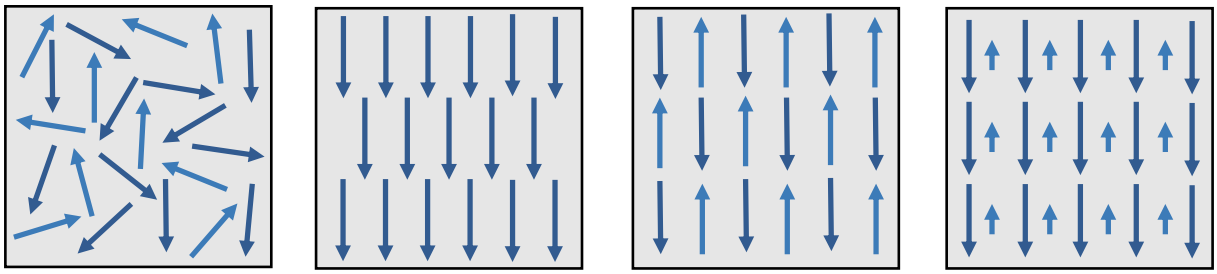

Figure 2.1: Illustration of magnetic moments ordering for different types of magnetic materials with no external fields. | **(a)** Paramagnet. The magnetic moments are randomly oriented and the net magnetic moment are zero. **(b)** Ferromagnet. The magnetic moments of the atoms are aligns parallel in one direction below a critical temperature, T_C. **(c)** Antiferromagnet. The magnetic moments of the atoms are aligns antiparallel, resulting in a net zero magnetization below the Néel temperature, T_N. **(d)** Ferrimagnet. Antiparallel ordering of magnetic moments of different magnitude, resulting in a net nonzero magnetization.

Ferromagnets, antiferromagnets, and ferrimagnets all have an intrinsic ordering of the magnetic dipole moments in the absence of external fields. In ferromagnets, the magnetic moments will align in the same direction as an applied magnetic field. However, in

contrast to paramagnetic materials, the magnetic moments stay aligned after turning off the external field. This characteristic makes ferromagnetic materials interesting for applications in spintronics, electronics, and biomedicine [14]. Antiferromagnets are similar to ferromagnets, as the magnetic moments tend to align in the same direction. However, the spins are aligned antiparallel in antiferromagnets, making the total net magnetization zero. Ferrimagnets are another type of magnetic material where antiparallel spin alignment is energetically preferred. Ferrimagnets are distinguishable from antiferromagnets as they have a small net magnetization. This is because the two antiparallel magnetic moments are of different magnitude.

2.1.4 Ferromagnetic Materials

Domain Theory

What we have discussed up until now suggests that all ferromagnetic materials will have a strong magnetic field because their magnetic moments are aligned in the same direction. However, bulks of ferromagnetic materials like iron are still found naturally in a state close to net-zero magnetization. An explanation is found when taking a closer look at the magnetic moments in a ferromagnetic bulk. The ordering inside ferromagnetic materials is limited to regions inside the material called domains. Each domain will have a saturated magnetization pointing in a particular direction. However, different domains will not necessarily point in the same direction. An example of such domains inside a ferromagnetic bulk material is shown in Figure 2.2.

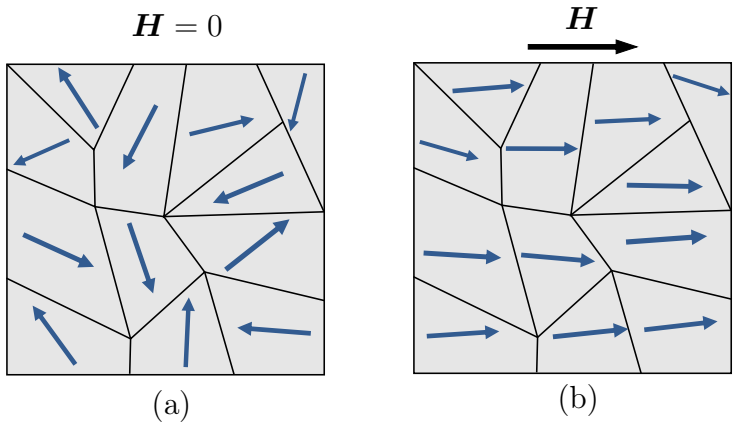

Figure 2.2: Domain formation in a ferromagnetic bulk | Each arrow represent the total magnetization its respective domain. **(a)** No external field is applied. In order to reduce the stray field, the domains are pointing in different directions. **(b)** An external field has been applied. The magnetic moments respond to this field by aligning in the same direction, and the bulk magnetization is almost saturated.

Initially, the magnetic moments of atoms in ferromagnetic materials align because of a short-ranged quantum mechanic effect called *exchange interaction*. As a result, two nearby

atoms with unpaired electrons will energetically favor parallel or antiparallel ordering of their spins. For ferromagnetic materials, parallel ordering is energetically favorable. However, if all the dipoles in the bulk were to align in the same direction, they would create a large magnetic *stray field* extending to the surroundings. Having a sizeable stray field is energy costly, and domains are created to reduce the energy. The trade-off between the different energies involved will decide the final domain formation. In a large bulk of ferromagnetic material, the energy cost of domain formation is justified to minimize the system's total energy.

Domain Walls

The boundaries between adjacent domains in ferromagnetic bulk materials are called domain walls. Typically the magnetization changes by either 90° or 180° from one side of the wall to the other. The essential characteristic of the domain wall is the domain wall width, which is determined by balancing competing energy contributions. The exchange energy favors parallel aligned spins, and therefore wide walls are preferred as the angle mismatch between the adjacent spins is small. However, other energy contributions, such as the magnetocrystalline anisotropy caused by favorable crystallographic directions and the demagnetization energy, which is related to the sample shape, will contribute to minimizing the domain wall width [12].

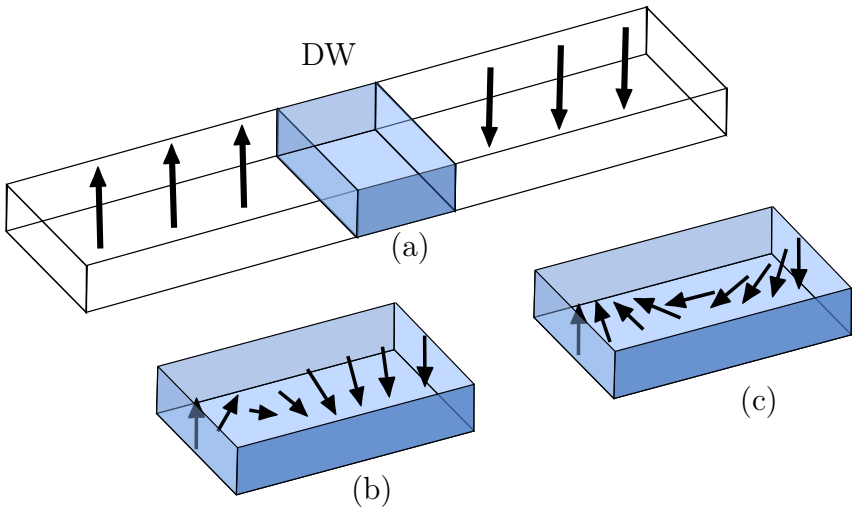

Figure 2.3: Schematic drawing of Bloch and Néel domain walls between two magnetic domains | **(a)** Two domains pointing in the opposite directions are separated by a domain wall (DW). Two possible domain wall structures may appear in the transition region, and the axis of rotation differentiates them. These are: **(b)** Bloch wall and **(c)** Neel wall.

Figure 2.3 display two possible domain walls between ferromagnetic domains. The first one is the Bloch wall, where the magnetization rotates in a plane parallel to the plane of the domain wall. The second one is the Néel wall, where the magnetization rotates in a

plane perpendicular to the domain wall plane. The energetically favorable domain wall in magnetic thin films is Néel walls. In Néel walls, free poles (or stray fields) are formed in the wall surface instead of the film surface, which reduces the magnetostatic energy [13].

Ferromagnetic Hysteresis Curve

The response of a paramagnetic material is linear, with a constant susceptibility, χ. The response of a ferromagnet is, however, a different story. Figure 2.4 shows what is called a hysteresis loop or hysteresis curve. Applying a magnetic field to a ferromagnet with net-zero magnetization (origo) will cause the magnetic moment to gradually align with the field until it reaches saturation magnetization, M_{S}. If the applied field then were to be turned off, one would think that the magnetization in the material also disappeared. The disappearance of the magnetization is not the case for ferromagnetic materials, as it still has some remanent magnetization, M_{R}, after the field is turned off. The magnetization does not go back to zero unless a field of particular strength is applied in the opposite direction, called the coercive field, H_{C}. The same behavior is observed in the opposite direction. We obtain the hysteresis curve by tracing the magnetization while switching the applied field back and forth.

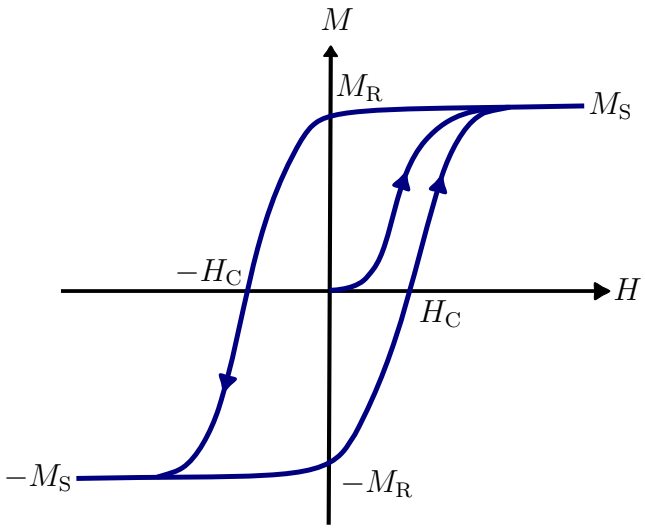

Figure 2.4: Example of a hysteresis curve for a ferromagnetic material | After applying sufficient field in one direction, the magnetization will saturate at M_{S}. When turning off the external field there will still be a remanent magnetization $M_{\mathrm{R}} \leq M_{\mathrm{S}}$. The magnetization switches when a field size of, $-H_{\mathrm{C}}$, is applied in the opposite direction.

Now we can take a closer look at the mechanisms behind the behavior of the ferromagnetic hysteresis curve and how domain formations influence it. When a magnetic field is applied to a piece of ferromagnetic material, the domains whose magnetization is closest to the applied field direction will start to grow at the expense of the other domains. The growth of single domains occurs by the motion of the domain walls. Domain walls in motion may

encounter imperfections such as defects or dislocations in the crystal. When this happens, the domain wall tends to relax at the imperfections, as these are energetically favorable positions. For the domain wall to move past the imperfection, energy is required. This energy can be provided by increasing the applied field. When turning off the magnetic field, there will still be some remanent magnetization M_{R} left in the material. The existence of a remanent field is evident because the demagnetization field created by the material is not strong enough to overcome the energy barriers when the domain walls encounter defects. The energy required to overcome domain wall pinning is of different magnitude across the sample. If the energy barriers created by imperfections are significant, the demagnetization process requires more energy, meaning that we get a sizeable coercive field [13]. In addition, domain wall pinning often yields a less steep jump in the hysteresis curve.

A microscopic consequence of domain wall pinning is an erratic movement of domain walls. The domain wall motion consists of periods of inactivity caused by pinning, followed by short bursts of movement as the domain wall(s) jump from one pinning site to the next. Three types of domain wall motion can be distinguished relative to the critical *depinning field* [15]. The motion below the depinning threshold is called *domain wall creep*. In this regime, the domain walls are mostly pinned. However, thermally activated motion from pinning sites occurs by random thermal fluctuations [16]. Around the depinning threshold, we have avalanches of domain wall motion as the depinning field is exceeded. This phenomenon is known as the Barkhausen effect. Figure 2.5 displays how the Barkhausen effect influences the virgin magnetization curve as a function of the applied field. After exceeding the depinning field, we are in the *flow* regime. In this regime, the applied field is sufficient to overcome most of the pinning effects, and the domain walls start moving steadily on average [15].

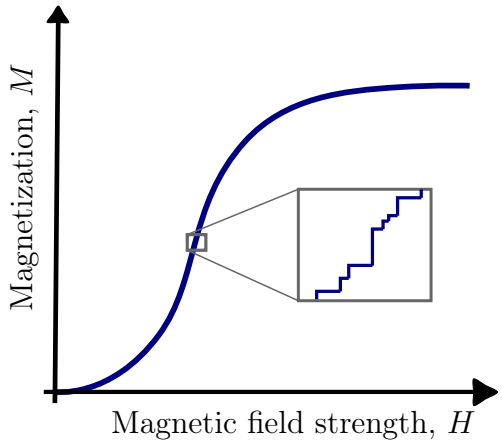

Figure 2.5: Barkhausen effect in virgin magnetization curve | Magnetization as a function of applied magnetic field strength in a ferromagnetic material. The inset shows sudden changes in the magnetization curve as the magnetic domains change when domain walls are depinned.

Another mechanism for the coercive field is domain wall nucleation. If we consider the ferromagnetic material in its saturated state, the magnetization in all the domains points in the same direction, and no domain walls exist. If a demagnetization field is now applied, domain walls must be nucleated before moving. Thus the domain wall nucleation can be the dominant mechanism. For a ferromagnet in its initial state, domain walls are already present in the material. Therefore, the need for domain wall nucleation is excluded, making domain wall motion and pinning the primary mechanism for the initial magnetization curve. A large squareness often characterizes magnetization reversal processes limited by domain wall nucleation. *Squareness* is defined as the ratio between the remanent magnetization and the saturation magnetization [17]. Suppose the remanent magnetization is equal to the saturated magnetization. In this case, the domain wall nucleation has not started yet, and an additional field is needed to begin domain wall motion.

2.1.5 Magnetic Anisotropy

Anisotropy in magnetic materials refers to direction dependence for the magnetic properties in the direction they are measured. The direction dependence means that the magnetic moments in many cases, will align at preferred axes to minimize the system's energy. There are many sources of anisotropy, and the two we will look into here are *magnetocrystalline anisotropy* and *shape anisotropy*.

The concept of magnetocrystalline anisotropy is the tendency of the magnetization to align with a preferred crystallographic direction. This material-specific property can be observed by applying a field along different crystallographic axes. As an example, body-centered Fe has a preferred magnetization axis along the $\langle 100 \rangle$ direction. We refer to this as the *easy* axis or the *easy* direction. In order to switch the magnetization to point along the *hard* axis, energy is required. This energy is called magnetocrystalline anisotropy energy. For Permalloy ($Ni_{1-x}Fe_x$), which is investigated in this thesis, the magnetocrystalline anisotropy is vanishingly small in the range of $0.18 \leq x \leq 0.25$ [18].

Shape anisotropy is a property that depends on the shape of the magnet. This effect is observed in magnetic thin films. Thin films have one limited direction, namely the direction perpendicular to the film. When a magnetic sample has a more significant extension in one direction, the magnetic moments prefer to align in the extended direction. Consequently, the moments in a magnetic thin film will align in the direction parallel to the plane. This behavior can be explained by the demagnetizing field, as shown in figure 2.6. The demagnetization field is more prominent when the moments point along the short axis and smaller when the moments point along the long axis. Having a large demagnetization field is energetically unfavorable since it corresponds to a higher magnetostatic energy [13].

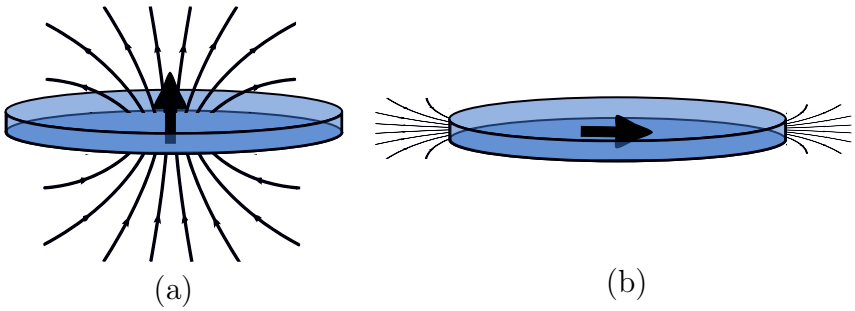

Figure 2.6: Shape anisotropy in a magnetic thin film | **(a)** A large energy costly demagnetization field is created when the magnetic moments align perpendicular to the thin film. **(b)** Moments prefer to align parallel to the plane as this reduces the demagnetization field.

2.1.6 Artificial Spin Ice

Artificial spin ices (ASIs) are typically built up by elongated ferromagnets in the nanoscale dimension. The nanomagnets are positioned systematically in 2D arrays allowing magnetic interactions. Therefore, their magnetization depends on the other magnets in the array and external fields. There exists an infinite amount of possible geometries and configurations for ASI, but one of the most researched ones is the square lattice displayed in figure 2.7 [19].

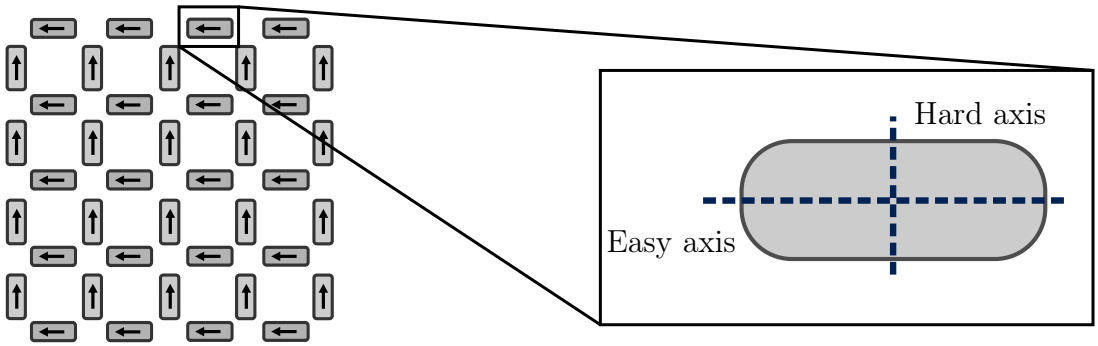

Figure 2.7: As seen from above, the square artificial spin ice and its building block | The square ASI is built up by elongated magnets. The nanomagnets are monodomain and inherit a strong shape anisotropy. The elongated axis is the easy axis for the magnetization, while the short axis is called the hard axis.

The anisotropy in the ASI building block is an important factor in the collective behavior of the system. The nanomagnets are small enough to be considered monodomain, meaning that all the magnetic moments will point in a given direction. The shape of the magnet introduces anisotropy. The nanomagnets are shaped with one short axis (hard axis) and one long axis (easy axis). The magnetization prefers to align against the easy axis, causing binarization of each magnet's spin states. The dimensions are typically $470\,\mathrm{nm} \times 170\,\mathrm{nm}$,

or even smaller [20]. The thickness of the magnets is small compared to the x- and y-dimensions (usually 10-20 nm), causing spin fluctuations in the z-direction to be negligible. The nanomagnet geometry is important for the anisotropy, and ASIs are usually fabricated on flat substrates when working experimentally. Using a substrate of high surface roughness will have consequences for the anisotropy of the magnets and unpredictable behavior.

2.2 Fabrication of Nanostructures

Lithography is the dominant technique for fabricating structures, such as artificial spin ice structures, down to the nanoscale. Lithography generally refers to the process of making a pattern on a substrate. Photolithography has, as a fabrication technique, had a major impact on the history of nanofabrication and made the creation of integrated circuits (ICs) down to the nanoscale possible. This has drastically influenced our everyday life by realizing the IC technology within our smartphones and laptops. Photolithography is also widely used in the research community, and in the work of this thesis, it is used to fabricate samples for vibrating sample-spectroscopy (VSM).

2.2.1 Photolithography

An example of how photolithography is used to transfer a pattern onto a substrate is shown in Figure 2.8. A substrate is first coated evenly with a material called photoresist. The photoresist is a light-sensitive material made up of a solvent, a sensitizer, and a polymer. When the photoresist is exposed to photons of specific wavelengths, the solubility of the resist will either increase or decrease based on the resist type. For a *positive* photoresists, the length of the polymer chains will be reduced when exposed to light, making it easier to remove the exposed areas with a developer. In the opposite case, the polymers in a *negative* photoresist will respond by cross-linking the polymer chains in the exposed areas [21]. Figure 2.8 displays a process using a positive photoresist. A designed pattern can be transferred to the substrate by selectively exposing certain parts of the photoresist.

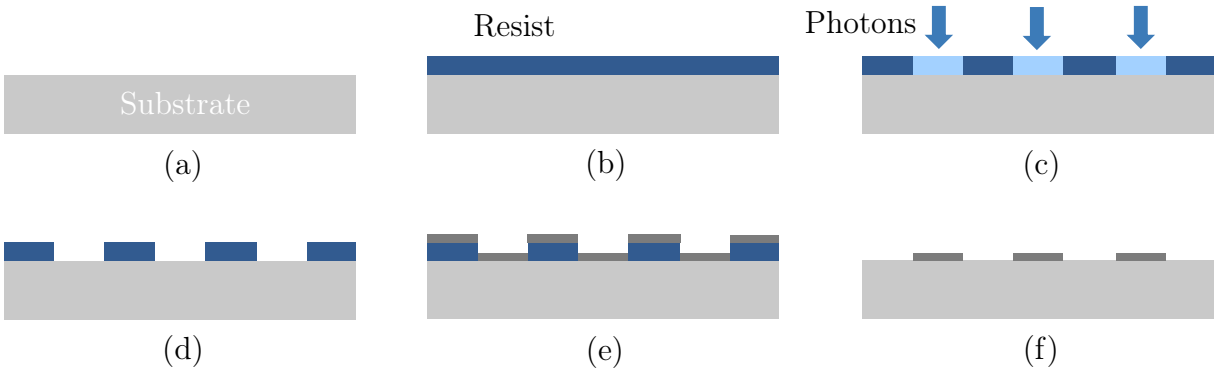

Figure 2.8: Illustration of a process that utilizes photolithography and lift-off | **(a)** A substrate with a clean and planar surface for patterning is cleaned before the process. **(b)** A thin layer of resist is deposited by spin coating. **(c)** A laser emits photons of a specific wavelength, exposing certain parts of the resist. **(d)** The exposed parts of the resist are removed by leaving the sample in a mixture called developer. **(e)** Metal is deposited on top of the sample. **(f)** Lift-off is performed, removing all the resist and the parts of the metal deposited on top of the resist.

Detailed Process Flow

Figure 2.9 displays the process flow in a typical photolithography process. The resist manufacturer often specifies the parameters for the steps, including spin coating and baking. However, the light intensity needed during exposure and the development time depends on the usage. In order to avoid exposure of the photoresist during lithography, photolithography cleanrooms are equipped with yellow LEDs containing no UV or blue light. Next, we will look closer into the sequence of steps included in one iteration of photolithography.

1. *Substrate cleaning.* In order to remove possible organic or inorganic contaminations on the surface, the wafer substrate must be cleaned. The removal is often performed by wet chemical treatment, using a solution such as acetone, methanol, and iso-2-propanol (IPA). Then the wafer is blown dry with N_2 gas. Plasma cleaning using O_2-plasma is an optional step for removing more of the organic material from the surface.

   Before moving on to spin coating, the substrate is heated on a hot plate to remove moisture from the surface. Dehydration improves the adhesion between the substrate and the hydrophobic photoresist.
2. *Spin coating.* The wafer is spun after applying the chemicals onto the surface to ensure a uniform layer of photoresist on the substrate. The thickness of the photoresist is controlled by changing the spin speed or the viscosity of the photoresist. The film gets progressively more uniform as it thins, and it will remain so for the duration of the process [22].

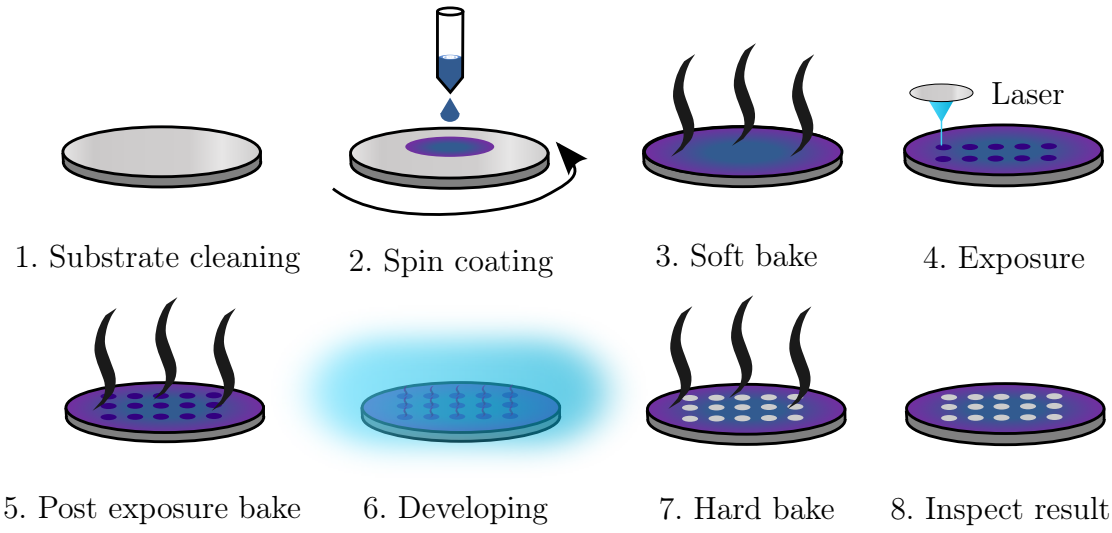

Figure 2.9: Sketch of the typical steps in a photolithography process | The three main steps are spin coating, exposure, and development. However, in most photolithography processes, all illustrated steps are performed to achieve a good result.

3. *Soft bake.* A soft bake is performed on a hot plate to remove solvent from the photoresist. The solvent's purpose is to make it easier to distribute the photoresist uniformly on the surface, and we want to evaporate it before moving on with the process.
4. *Exposure.* In order to transfer the designed pattern onto the photoresist, certain parts of the sample are exposed to laser light of specific wavelengths, typically in the UV regime.

   One can either use a mask-aligner or a maskless aligner. A mask-aligner utilizes a physical pre-made mask. The light is transmitted through the open areas on the mask, making it a fast method that is preferably used in large-scale productions. A maskless aligner utilizes mirrors and lenses to focus the UV light on specific parts of the sample. This method is slower but more versatile as you do not have to prepare and change masks. Maskless aligners are therefore preferred within research communities.
5. *Post exposure bake* (PEB). PEB is performed after exposure and helps enhance the solubility differential between unexposed and exposed areas by thermally activating the crosslinked polymer chains [23].
6. *Development.* A developer solution is used to remove the photoresist parts, which are soluble after exposure. The remaining photoresist will stay on the surface after development.
7. *Hard bake.* In order to ensure a stable resist and remove additional solvent from the wafer, the wafer is placed on a hot plate.

8. *Inspection.* The process is complete, and the wafer can be inspected to ensure an excellent final result.

2.2.2 Thin Films and Metallization

Thin films are generally used to enhance the surface properties of solids. As we have seen earlier, permalloy thin films are used in ASI structures by utilizing the anisotropic characteristics in the magnet. In general, metallic thin films are heavily used in the semiconductor industry and are highly important in integrated circuits. Technologies for thin film fabrication can be divided into chemical vapor deposition (CVD) and physical vapor deposition (PVD). Here, we will examine some of the metallization techniques belonging to the PVD family of processes.

PVD techniques deposit molecules or atoms onto a substrate from the vapor phase. These processes must be performed in vacuum chambers for the thin films' reproducibility, uniformity, and purity. A significant influence of residual gases means many collisions before the metal atoms hit the substrate and can force the gas molecules to be trapped inside the thin film. Electron beam evaporation and sputtering are two commonly used PVD methods. Figure 2.10 provides a schematic illustration of the processes inside the vacuum chamber for the two techniques. They both involve shooting atoms towards a rotating substrate.

E-beam evaporation is performed by bombarding the target material with an electron beam. Thermionic emission gives electrons off a tungsten filament and accelerates them towards the target. The electrons cause evaporation at the target material's surface, where the beam hits. While in the vapor phase, the target atoms spread out and deposit on the chamber walls and the substrate. The vapor will also deposit onto a quartz crystal that monitors the deposition rate. By raising or lowering the electron beam current, the deposition rate can accordingly be increased or decreased until the desired deposition rate is achieved.

The sputtering process is used extensively in the semiconductor industry to fabricate integrated circuits. Instead of electrons, the sputtering process utilizes ionized gas to eject atoms from the target. Argon gas is often used as it is an inert gas. The main advantage of this technique is that it works for materials with a high melting point, where E-beam Evaporation can be problematic [24].

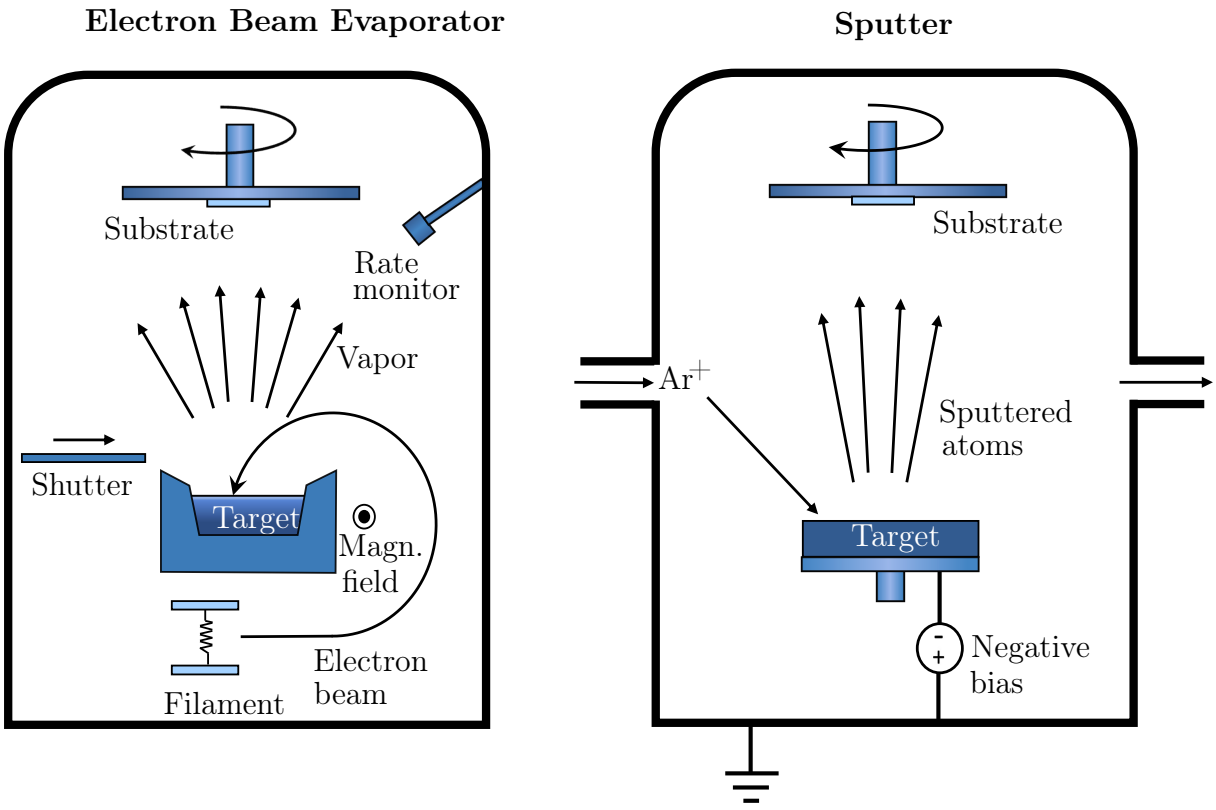

Figure 2.10: Schematic illustration of the E-beam Evaporator and the sputtering system. | Both deposition processes occur inside a vacuum chamber. The substrate is spinning during deposition to enhance uniformity.

Spitting

When depositing material by evaporation from a molten target, there is a possibility that tiny droplets are ejected. In order to achieve a smooth and uniform thin film, vapor from the molten pool should be emitted. However, when liquid droplets are ejected, they will travel along with the vapor in the vacuum chamber and deposit onto the mounted sample, where it solidifies. This phenomenon is called spitting and is commonly caused by the release of vapor from inside the molten target [25]. Figure 4.2 displays a visual representation of the effect. Spitting is a problem for thin film applications since it ruins the topographic thin film properties and can cause short-circuiting in integrated circuits applications. There are several ways of preventing spitting from happening. One way of reducing the risk of spitting is to change the target material into one of higher purity. Another parameter that can be adjusted to minimize spitting is to prevent rapid heating by adjusting the electron beam current more gently.

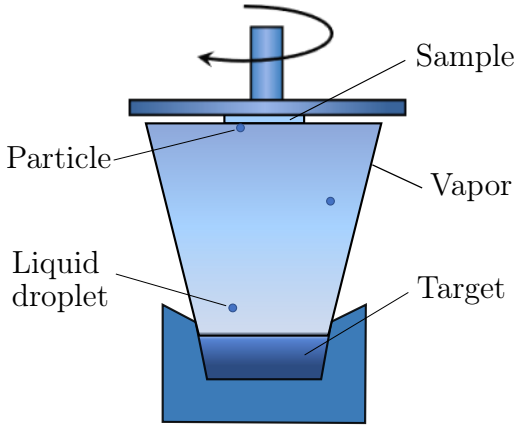

Figure 2.11: Illustration of spitting occurring inside an E-beam evaporator | Small droplets of liquid material are ejected from the target alongside the vapor when the target is heated. The droplets form solid particles when deposited on the spinning sample's surface.

Oxidation of Metal Thin Films

When metal surfaces are in contact with an oxygen atmosphere, the formation of oxide scales will occur [26]. The oxidated metal is typically written as M_xO_y, where M is the metal and O is oxygen. As thin films get thinner, the surface-to-volume ratio increases, making the effects of oxidation more prominent. The ferromagnetic alloy, permalloy ($Ni_{0.8}Fe_{0.2}$), is one of the most common materials found in a variety of magnetic micro- and nanostructures [27]. Permalloy (Py) is also the ferromagnetic material of choice for this thesis. When Py is exposed to air, corrosion occurs. Iron oxides and nickel oxides form a thin oxide layer on the surface, making the rest of the Py thin film corrosion resistant as the oxidized layer protects the rest of the film. However, Py loses its ferromagnetic properties once oxidized. The metal oxides inherit other magnetic properties than the original alloy, and NiO will even become antiferromagnetic [28]. In order to prevent the formation of Py oxides, a thin passivation layer of Al is often deposited on top of the Py surface. Al will form a passivation layer when exposed to air, shielding the Py thin film underneath from further oxidation.

2.3 Characterization Techniques

2.3.1 Scanning Electron Microscopy

The scanning electron microscope (SEM) is an essential tool for the topological characterization of nanometer- and micrometer-sized structures. The SEM operates at high voltages, utilizing a focused electron beam and the electron's scattering mechanisms. The images are acquired by scanning the material's surface with the electron beam while simultaneously detecting the signals they create when interacting with the sample.

High-energy primary electrons penetrating the sample from above will interact with the atoms in the sample and their surrounding electrons. Two different types of scattering occur in the solid, inelastic and elastic scattering, which are both displayed in Figure 2.12. The atoms in the sample are several thousand times heavier than the electron. When electrons collide with the atoms, their energy will be preserved, and they change direction by a scattering angle. This interaction leads to either forward scattering (small scattering angle) or back-scattered electrons (large scattering angle). Electron-electron interactions are inelastic. The incoming (primary) electron loses some of its momenta to break free a secondary electron (SE) [29]. The SE's energy will be much lower than the energy of the primary electron. However, SEs are highly important when imaging surfaces since only the electrons near the surface manage to escape from the sample.

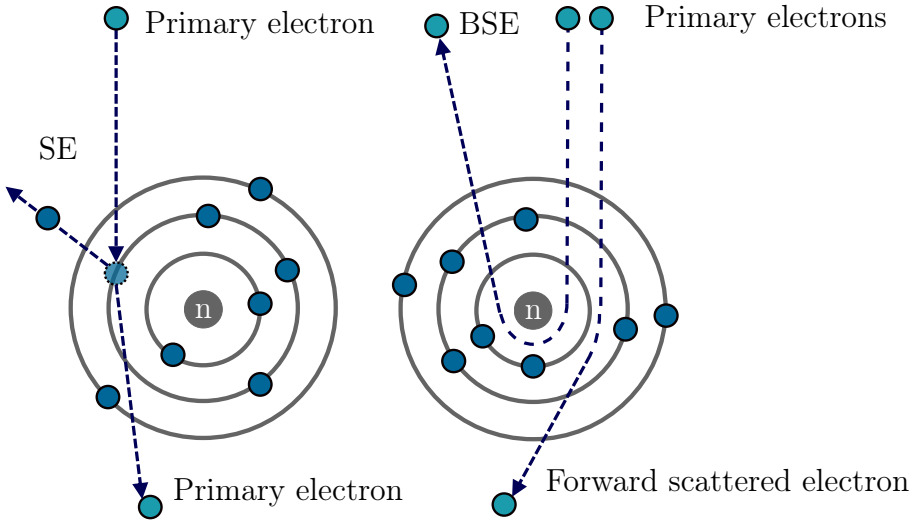

(a) Ineastic scattering (b) Elastic scattering

Figure 2.12: A pictorial description of how incoming electrons interact with atoms | High-energy primary electrons interact through two basic scattering mechanisms. **(a)** Inelastic scattering where the primary electron loses some of its energy to break free a secondary electron. **(b)** Elastic scattering occurs when the primary electron interacts with the heavy nucleus. The primary electron is either back-scattered or forward-scattered while preserving its energy.

Most SEMs are equipped with an Everhart-Thornley detector (ETD), placed in the vacuum chamber with the sample. The ETD detects low-energy SE. Many SEMs also have in-lens detectors for both BSE and SE. As the electron beam scans the surface, the detectors measure the number of SE or BSE that has been excited. The signal intensity for each spot can be converted into a grayscale value which makes up the final image of the surface. The intensity of the signal will vary as the surface gradient changes, making it possible to image surface features in great detail. Its capability of capturing images with a resolution down to a few nanometers has made the SEM an excellent tool for characterization [30].

2.3.2 Atomic Force Microscopy

Atomic force microscopy (AFM) is a scanning probe microscopy technique aiming to obtain a topographic map of the sample surface. The working principle is relatively simple yet extremely delicate. The ultra-sharp tip placed at the end of a cantilever scans the x- and y-direction of the sample surface while containing proximity to the sample surface. The sharpness of the tip goes down to a singular atom allowing it to experience the force of atom-atom interactions at the surface, thus obtaining sub-nanometer height resolution. The resolution in the lateral direction is limited by the cantilever movement, which is often controlled by piezo-motors. As shown in figure 2.13, a laser is aimed at the top of the cantilever and reflected onto a quadrant detector. While scanning the surface, the cantilever is oscillating at a particular frequency. The detector measures changes in the laser's frequency, deflection path, and phase. In order to restore the response signal, the height of the cantilever is adjusted [31]. The height profile information at the sample surface is thus stored and can be exported as a .spm file.

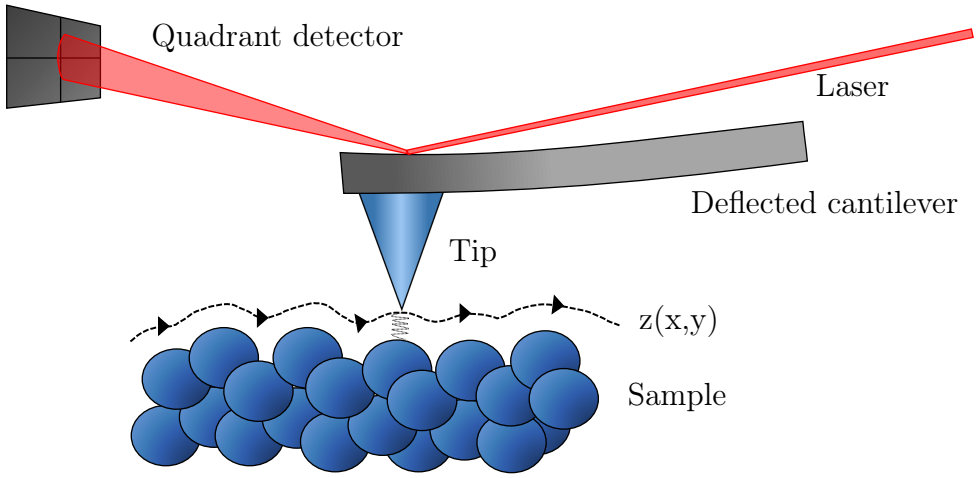

Figure 2.13: Schematic illustration of the AFM | While scanning the surface, a laser is reflected off the oscillating tip onto the quadrant detector. Based on the readings from the detector, the cantilever can adjust its height. The tip will thus track the height of the sample surface, providing the $z(x, y)$ data.

The AFM has, through the years, proven to be a reliable tool for surface measurements. In addition to surface topography, the AFM can measure ferroelectricity, piezoelectricity, and magnetic moments. The different modes require different AFM tips, which can be easily changed. The AFM does not need sample preparations and can operate under ambient conditions. Consequently, AFMs now exist in university and industrial laboratories all over the world [31].

Surface Roughness Parameters

Software for visually representing the gathered surface profile provides a powerful foundation for surface characterization. However, critical parameters that describe the roughness of the surface can also be derived from the AFM data. These include *height parameters* and *amplitude distribution function parameters*. By obtaining these parameters, different surfaces can be compared quantitatively [32].

Two of the most used representations for surface roughness in the literature are the root mean square (rms or S_q) and the arithmetic average (S_a). These are height parameters based on height deviations from the mean plane, $Z(x, y)$. rms calculations are also used in other disciplines, such as electrical engineering. The continuous and discrete formula for the rms roughness (S_q) is given by:

$$S_\mathrm{q} = \sqrt{\frac{1}{A}\iint_A Z^2(x,y)dxdy} \tag{2.6a}$$

$$S_\mathrm{q} = \sqrt{\frac{1}{N}\sum_{i=1}^{N} Z_i^2} \tag{2.6b}$$

A is the evaluation area, and N is the number of evaluated data points. Scanning probe microscopy techniques such as AFM acquire a discrete set of information about the x, y, and z positions, and the discrete formula is used when evaluating experimental results.

The Sa value can be determined with a slightly different formula.

$$Sa = \frac{1}{A}\iint_A |Z(x,y)|dxdy \tag{2.7a}$$

$$Sa = \frac{1}{N}\sum_{i=1}^{N} |Z_i| \tag{2.7b}$$

Examination of the equations tells us that S_a will have a relatively low response to one prominent peak or flow in the sample compared to the rms value. For applications where the surface needs to be flat and uniform, low values for S_a and S_q are preferred.

Amplitude distribution function parameters can function as supplementary information to portray the surface roughness. These unitless parameters are skewness (S_sk) and kurtosis (S_ku). These values are calculated through the discrete equations:

$$S_\mathrm{sk} = \frac{1}{Sq^3}\left[\frac{1}{N}\sum_{i=1}^{N} Z_i^3\right] \tag{2.8a}$$

$$S_{\text{ku}} = \frac{1}{Sq^4}\left[\frac{1}{N}\sum_{i=1}^{N} Z_i^4\right] \tag{2.8b}$$

These equations are harder to interpret directly, but figure 2.14 offers visual profile descriptions of their nature for different types of surface profiles. Skewness is a measure of symmetry about the mean line. For example, a valley-rich surface with longer obtuse peaks will have a negative skew. Subsequently, a surface dominated by peaks will have positive skewness. The kurtosis measures how sharp the surface spikes are and how uniform they are about the mean line. Typically a kurtosis value greater than 3 indicates a spiky surface, whereas surfaces with kurtosis values lower than 3 are more "bumpy" [33]. It is common to compare the excess kurtosis, defined as $S_{\text{ku}} - 3$. The excess kurtosis is therefore normalized around 0 instead of 3. In this thesis, the results will be presented in terms of excess kurtosis.

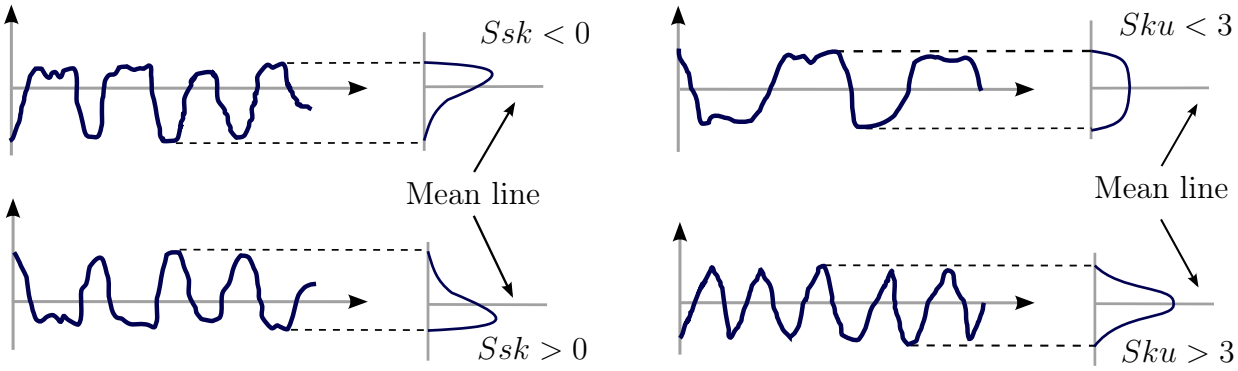

(a) Skewness (b) Kurtosis

Figure 2.14: Profile descriptions of the roughness parameters skewness and kurtosis | Profiles are exaggerated to represent how the parameters vary visually. **(a)** Skewness measures symmetry about the mean line. An even distribution about the mean line would have resulted in $S_{\text{sk}} = 0$. **(b)** Kurtosis above 3 indicates a spiky surface in the evaluation area. The kurtosis value drops below 3 if the surface is less spiky.

2.3.3 Vibrating-Sample Magnetometry

A vibrating-sample magnetometer (VSM) is an instrument typically used to measure a sample's magnetic moment in response to an external field [34]. The sample is placed on a long rod and led down inside an electromagnet, as shown in Figure 2.15. The magnetic moment of the sample will align with the field created by the electromagnet to minimize its energy. To detect the magnetization of the sample, a linear motor is used to move it up and down. The magnetic field created by the magnetic moment of the sample will change with regard to time while vibrating. This alternating magnetic field induces an electric current in the detection coil. By measuring the current in the magnetic coils, the magnetization of the sample can be calculated through Faraday's law of induction [35].

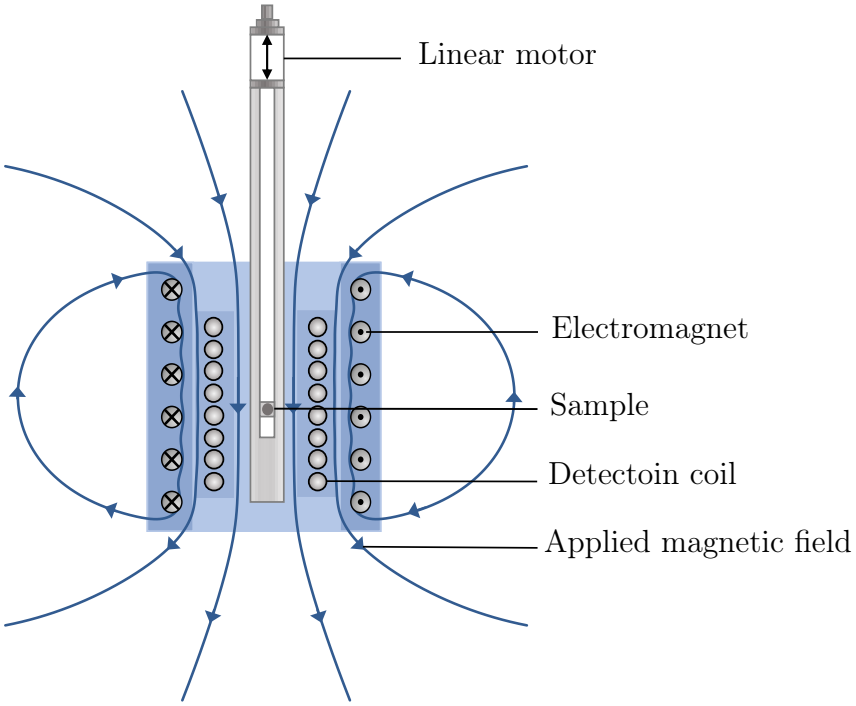

Figure 2.15: Schematic description of the essential parts of the VSM | Sample is placed inside the magnetic field set up by an electromagnet. The linear motor is causing the sample holder to vibrate. The vibration creates an alternating field from the sample's magnetization, which the detection coil picks up.

If a sample is vibrating at a frequency f, the induced voltage E in the detection coil is given by

$$E = \sigma A G 2\pi f \cos(2\pi f t), \tag{2.9}$$

where σ is the magnetic moment of the sample, A is the amplitude of the sinusoidal vibrations, and G is a factor that depends on the detection coil geometry [36]. Using Equation 2.9, magnetization values can be found for discrete magnitudes of the applied field, and thus the hysteresis curves of ferromagnetic samples are obtained.

Chapter 3

Experimental Procedure

The first section of this chapter will present the design and fabrication process and an overview of all the samples investigated. The following section will present the relevant characterization tools that have been employed in this thesis, in addition to relevant computer software for processing the gathered data.

3.1 Fabrication of Samples

The fabrication process starts out with 2" silicon wafers with a crystal plane orientation of <100> ±1°. The goal is to produce permalloy ($Ni_{0.8}Fe_{0.2}$) thin films on top of metal thin films of varying roughness. The fabrication process can be divided into four steps as described in Figure 3.1. The first step is evaporating a layer of non-magnetic metal on the silicon wafer, creating an uneven surface on the substrate. The next step is photolithography, where the wanted pattern is transferred onto the wafer. This is followed by a new round of metallization, where the magnetic permalloy is evaporated onto the surface. In order to remove the photoresist and excess material, lift-off is performed. Lastly, the individual VSM samples are extracted from the wafer by scribing.

3.1.1 Sample Design

There are two main concerns when choosing the design for VSM samples. Firstly, the samples must be cut in dimensions less than 4 mm × 4 mm in order to fit on the VSM sample holder. Secondly, the samples should be identical and symmetrical. The symmetry eliminates the effect of shape anisotropy in our measurements. A sample design that would fit these requirements was circular discs with a diameter of $d = 3500\,\mu m$. By choosing a diameter shorter than 4 mm the additional space prevents the discs from being damaged in the scribing process. With circular discs, there is no shape anisotropy to take into account when performing the measurements, making it easier to compare different samples. The

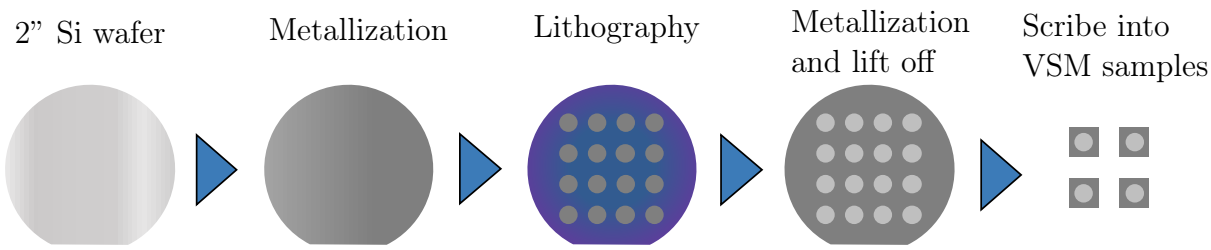

Figure 3.1: Visual description of the fabrication process | VSM samples are fabricated using 2” <100> Si wafers. First, a metal layer is deposited on the surface to achieve a certain surface roughness. The pattern is transferred to the sample by photolithography. When the pattern is ready, magnetic material (permalloy) is deposited. After performing lift-off, we are left with circular permalloy structures on the wafer. Finally, scribing separates these circular discs of permalloy into individual VSM samples.

lithography design was realized using the python package PHIDL [37]. The created design was simply an array of circular shapes, utilizing the space available on the silicon wafer.

3.1.2 Metallization

Metallization was performed using two E-beam evaporators (EBEs) capable of both single and multilayer thin films. The first round of metallization directly on the Si wafer was performed with the *E-beam evaporator and Sputter AJA*. As the name suggests, the AJA can perform e-beam evaporation and sputtering. The available materials can be changed on demand by a cleanroom engineer. For this thesis, the materials of interest were Ti, Au, Cu, and Al. All of these materials were available on the AJA. In order to obtain metal layers of varying roughness, the deposition thickness or rate was systematically changed between the depositions.

The second round of metallization in the sample fabrication process took place after photolithography to deposit the magnetic permalloy ($Ni_{0.8}Fe_{0.2}$). In addition, a thin Al layer was deposited to reduce the risk of oxidation at the permalloy surface, leading to loss of magnetic properties. These two layers were deposited manually using Pfeiffer’s Vacuum Classic 500 E-Beam Evaporator. The instrument relies on a more manual process which requires the user to control and maintain a steady increase of the electron beam current until reaching the wanted deposition rate. When a steady rate is established, a mechanical shutter is controlled manually to accomplish the proper thickness. All deposited permalloy layers in this thesis had a thickness of 20 nm with a 2.5 nm thick Al protection layer on top.

3.1.3 Photolithography

Photolithography was performed on the prepared substrates with different surface roughness values, followed by lift-off and scribing. The work was done in NanoLab at NTNU

Campus Gløshaugen. The exposure was performed using the MLA150 Maskless Aligner from Heidelberg Instruments.

In order to optimize the lithography process and minimize fabrication errors, dose and development tests are usually performed prior to the fabrication process. Thankfully, dose and development tests were carried out before this thesis. Therefore, the procedure was unnecessary. Generally, using a negative resist is preferred when lift-off is performed after photolithography. Despite this, the positive photoresist MEGAPOSIT™SPR™700-1.0 (SPR700) was chosen for the process. SPR700 is a consistent photoresist that forms a 1 µm thick layer after spin coating. The resist layer is quite wide compared to the 22.5 nm thick Py/Al layer deposited on top, making lift-off easier. The chemical used as the developer was ma-D 332 mixed with deionized water in a 2:1 ratio. Table 3.1 displays the list of process parameters that were used based on the SPR700 datasheet and previous dose, and development tests [38, 39].

Table 3.1: Description of all process steps and relevant parameters during photolithography with SPR700 positive photoresist.

Process step	**Detailed description**
Substrate preparation	Rinse with acetone, then IPA. Blow dry with nitrogen. Plasma cleaning, 10 minutes at 600 sccm O_2 and 1000 W
Dehydration bake	5 min at 150 °C.
Spin coating	34 sec at 4000 rpm Acceleration of 1000 rpm/s
Soft bake	1 min at 95 °C
Exposure dose	120 µC/cm^2
PEB	1 min at 115 °C
Developing	ma-D 332:DI water 2:1 Rinse with DI water. Blow dry with nitrogen.

The photolithography process is followed by lift-off to remove the photoresist and excess material. Lift-off was performed using acetone in an ultrasonic bath for 2-3 min, then rinsed with IPA and DI-water. Inspection using a light microscope revealed that the process had to be carefully conducted to avoid excess material from attaching to the surface. In the worst case, these tiny pieces, barely visible to the human eye, could influence VSM measurements. By lifting the wafer diagonally out of the acetone while splashing generously using an IPA squirt bottle, the amount of residue was reduced to a minimum.

3.1.4 Overview of Samples

Table 3.2 displays a list of all the relevant samples discussed in this thesis. The fabricated samples can be divided into two different categories. The first category contains gold films. Unfortunately, the Au films were not suited for VSM samples as particles were deposited at the surface due to spitting. However, the other category contains samples with Ti/Cu/Al layers of different thicknesses with fabricated permalloy disks on top, as shown schematically in figure 3.2. These samples were fabricated to identify how the roughness affects the hysteresis curves from the permalloy thin films.

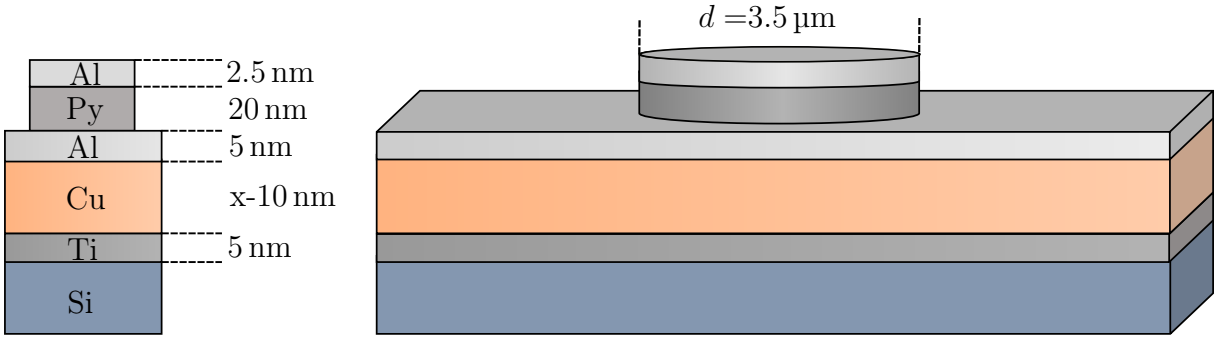

Figure 3.2: Illustration of the metal layers of VSM samples | The thickness of each metal layer is indicated and not to scale. Samples of varying thicknesses of the Cu layer were fabricated. The varying thickness is indicated by the $x - 10\,\text{nm}$ thick Cu layer, where x is the total thickness of the Ti/Cu/Al stack.

3.2 Characterization

3.2.1 Surface Topology Measurements

The AFM images were obtained with AFM Dimension Icon using both SCANASYST-AIR probes from Bruker. The triangular cantilevers on these probes are made of silicon nitride. The scans are performed in ScanAsyst mode, and the scan areas are squares with lengths of 2 µm on the sample surfaces. For each sample, three scans were performed at different locations to obtain more precise results. The scan rate was set to 1-2 Hz, and the number of imaged points per scan line was set to 512. The ScanAsyst mode makes imaging easier since the algorithms continuously monitor image quality and make appropriate parameter adjustments [40].

Processing AFM Data

The obtained .spm files from AFM characterization were later processed and analyzed using the open-source SPM data analysis software Gwyddion. Gwyddion allows reproducible data-processing routines that filter instrumental errors and noise [41]. It can also

Table 3.2: A list containing the fabricated samples for the work of this thesis. In order to avoid giving all the information about the sample in the discussion, they are assigned simple names. All thin films are fabricated on <100> oriented 2" Si wafers. The "metal layers" column contains layers deposited before the lithography process. The "magnetic layers" contain information about the magnetic material and the capping layer deposited after photolithography.

Sample name	**Metal layers**	**Evaporation rate**	**Magnetic layers**
Au 1 Å/s	5 nm Ti 145 nm Au	5 Å/s 1 Å/s	None
Au 3 Å/s	5 nm Ti 145 nm Au	5 Å/s 3 Å/s	None
Au 5 Å/s	5 nm Ti 145 nm Au	5 Å/s 5 Å/s	None
Au 7 Å/s	5 nm Ti 145 nm Au	5 Å/s 7 Å/s	None
Cu 0 nm	None Si wafer	———	20 nm Py 2.5 nm Al
Cu 50 nm	5 nm Ti 40 nm Cu 5 nm Al	5 Å/s 5 Å/s 5 Å/s	20 nm Py 2.5 nm Al
Cu 100 nm	5 nm Ti 90 nm Cu 5 nm Al	5 Å/s 5 Å/s 5 Å/s	20 nm Py 2.5 nm Al
Cu 150 nm	5 nm Ti 140 nm Cu 5 nm Al	5 Å/s 5 Å/s 5 Å/s	20 nm Py 2.5 nm Al
Cu 50 nm Batch 2	5 nm Ti 40 nm Cu 5 nm Al	5 Å/s 5 Å/s 5 Å/s	20 nm Py 2.5 nm Al

create two- and three-dimensional images of the surface and calculate roughness parameters based on the data. This allows both quantitative and visual representations of the sample surface.

The AFM data-processing was performed stepwise in Gwyddion. The first step in the process was to level the data by mean plane subtraction. Next, horizontal scan lines were aligned by subtracting a zero degree (mean line) polynomial from each row. Lastly, correction of scars was performed. Scars are common scanning errors and can easily be removed using neighbor lines as an estimation.

Grain Size Data

In order to obtain knowledge about the grain size distribution for the thin films, a watershed algorithm in Gwyddion was used. Grain segmentation can be performed in different ways, but the watershed algorithm can be used effectively for more complicated structures. The algorithm can be divided into two steps:

1. Grain location phase.
2. Segmentation phase.

In the grain location phase, virtual water droplets are placed in each data point for the inverted surface. These droplets will follow the steepest descending path to minimize their potential energy. Each droplet will end up in a local minimum, filling the inverted surface. Minima below a specific threshold value will be treated as instrumental errors and discarded. The minima will be evaluated as individual grains.

The segmentation phase involves finding the size and extent of the marked grains. This is done by continuously adding water droplets to the surface, making them fill the basins surrounding the local minima. These basins will eventually mark the area of each grain on the surface. The amount of added virtual water on the surface is controlled by a drop size parameter. Figure 3.3 describes how the grains change when adjusting this parameter. In this thesis, a drop size value of 100 % was used in order to be sure to mark the whole grains. In addition, a threshold value of $100\,\mathrm{nm}^2$ was set to remove grains caused by instrumental errors. When talking about grain size in other sections, the values are based on the projected area each grain produces. The grain diameter, d, is calculated by considering the grain as a circle of the same area.

Tip Convolution and Broken Tips

Since we are not dealing with an ideal world where AFM tips are shaped like delta functions, a degree of distortion due to tip convolution can be observed in surface images. Despite this fact, the AFM probes trace the surface of the thin films studied in this thesis quite well. More minor surface features than tip dimensions will produce less accurate sample images. Since the features on the thin films are significant compared to the

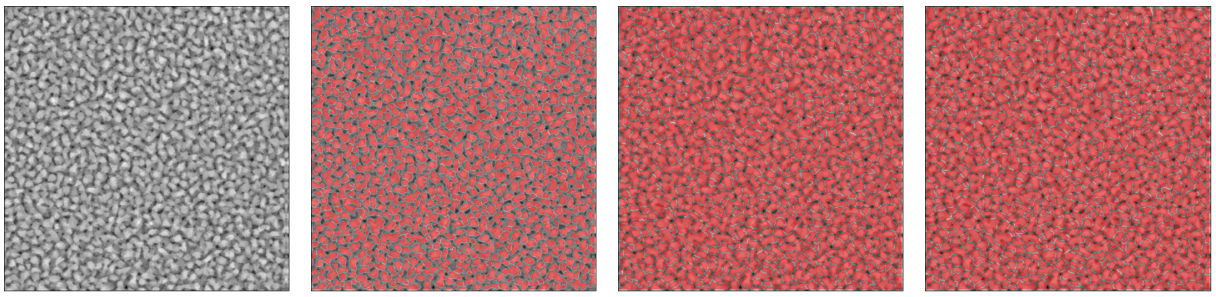

(a) (b) (c) (d)

Figure 3.3: Marking of grains by varying drop size parameter | The drop size parameter controls the amount of "virtual water" in the watershed algorithm. The red areas marks individual grains with the drop size parameter set to **(a)** 0 % **(b)** 20 % **(c)** 60 % **(d)** 100 %. The AFM image is based on a 2 µm×2 µm scan area.

sharpness of the AFM tip, convolution is not a significant problem.

However, AFM tips can be progressively dulled or damaged, causing convolution effects to be more pronounced. When the tip area increases, the shape of the tip will dominate the shape of the features on the sample surface. Figure 3.4a displays images taken with a broken probe, and Figure 3.4b displays an image from the same surface when using a new and well-functioning probe. The broken probe produces triangular shapes, all pointing in the same direction. The triangular shapes are measured because the imaged structures will have the same shape as the cross-section of the SCANASYST-AIR probes but rotated by 180 degrees. Knowledge about the surface structure of the thin film and tip convolution can prevent the usage of poor AFM images so that these are not interpreted as the actual surface morphology.

3.2.2 Microscopy Techniques

The fabricated structures were evaluated using a scanning electron microscope (SEM) and an optical microscope. High-resolution images of the surface were obtained using the SEM APREO from FEI. It is equipped with two in-lens detectors and one ETD detector. The in-lense T2 detector primarily designed for detecting secondary electrons was used to obtain the images. In order to ensure high-resolution images, immersion mode was used with a beam voltage of 2 kV, a beam current of 25 pA, and a working distance (WD) of 3-4 mm. Obtaining these conditions while maintaining a focused electron beam on the sample surface is difficult. A good approach is to begin at a WD of 10 mm and a beam current of 0.1 nA, and then proceed towards the optimal conditions while continuously adjusting the focus, stigma, contrast, and brightness. Immersion mode requires magnetic lenses and should not be used on magnetic samples [42]. Therefore, optiplan mode was used with great results under the same working conditions when imaging magnetic samples. The Zeiss AxoScope A1 from Carl Zeiss was used for optical imaging of surfaces.

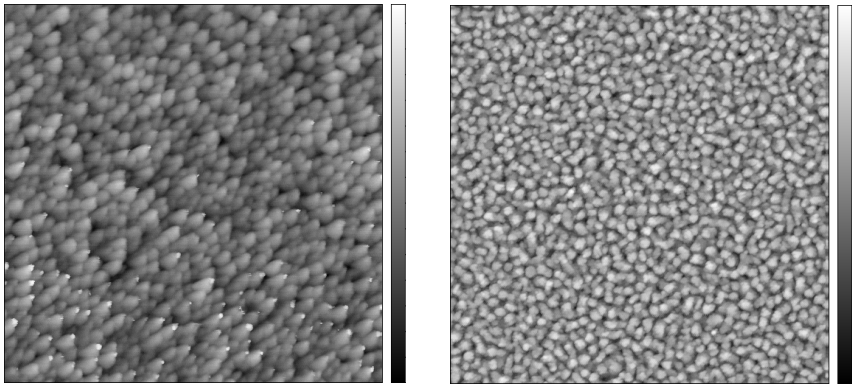

(a) (b)

Figure 3.4: Two AFM images of the same surface were obtained using two different probes | The images are based on two sets of AFM data from the same CuAl thin film surface. Both images are captured using Scanasyst-air probes. **(a)** Image is obtained using a broken AFM tip. The shape of the grains is distorted to triangular shapes, and the top to bottom height difference is decreased. **(b)** Image of the same sample surface obtained using a brand new AFM probe. The image is a much better representation of the actual surface topology, and the grains do not have a triangular shape. The height scales in the images are **(a)** 7.36 nm and **(b)** 11.0 nm and the scan areas are squares with a side length of 2 µm

3.2.3 VSM Measurements

The VSM measurements were performed with a Quantum Design Versalab system with a VSM module [43]. The samples were mounted with non-magnetic gum resin onto a glass sample holder, and a mounting stage was used to ensure correct positioning. The samples were carefully inserted into the VSM chamber before purging and sealing with He. The samples were mounted, so the magnetic field was applied parallel to the sample surface. The sample position inside the chamber was determined by performing a detection sequence where the applied field was set to 2000 Oersteds (Oe). The position where the strongest magnetic signal was detected determined the sample position. Then, measurement sequences covering the whole hysteresis loop of the sample were run, typically covering an interval from $H \in [-50, 50]$ Oe. The field increment was set to 0.3 Oe, with an averaging time of 1 s. The measurements were performed at a temperature of 300 K and a chamber pressure of 50 Torr. The Versalab system does not allow automatic rotation inside the vacuum chamber. Therefore, to measure the samples at different angles, they had to be rotated manually on the sample holder by reattaching the samples at a different angle. The samples were measured at two angles perpendicular to each other.

Noise and Data Filtering

The raw data gathered from the VSM measurements contain the hysteresis profile of the sample in addition to noise in the order of the listed resolution limit of 10^{-6} emu [44].

In order to gather essential parameters from the hysteresis measurements, the data needs to be filtered. Both the saturation magnetization, M_S, and coercive field, H_C, can be determined more reliably if the data is filtered first.

The hysteresis data filtering was performed using a Savitzky-Golay (S-G) filter from the python package scipy [45]. The Savitzky-Golay filter is a smoothing filter for digital data that increases precision while preserving signal tendency. The linear least-squares method is used on successive sub-sets of $2M+1$ adjacent data points with a low degree polynomial. The sub-set of $2M+1$ data points is used to evaluate the middle point of the group. After evaluating one point, a new group of $2M+1$ points is chosen by shifting the analysis interval one step to the right. It has been shown by Savitzky and Golay that the smoothed output value of the fitted polynomial is identical to a fixed linear combination of the set of input points [46]. Each smoothed variable is therefore calculated by a discrete convolution given by

$$y_{smoothed,j} = \sum_{i=j-M}^{j+M} C_i y_{j+i}, \tag{3.1}$$

where C_i comes from a fixed set of $2M+1$ weighting coefficients. After experimenting with different parameters, an S-G filter with $M = 5$ and degree 1 was chosen to smooth the experimental hysteresis curves. The vital characteristic for the parameter choice was the smoothness on the top and bottom of the hysteresis curve, making a degree 1 polynomial suitable to remove the noise. Figure 3.5 displays a raw hysteresis curve together with the resulting S-G filtered hysteresis curve.

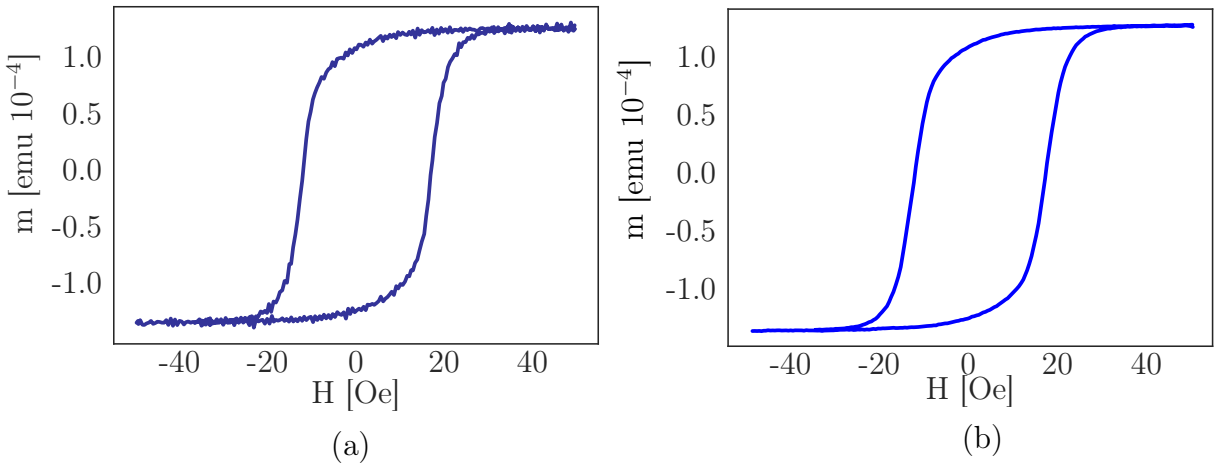

Figure 3.5: Unfiltered and S-G filtered hysteresis curves | **(a)** Raw data gathered from a VSM measurement. **(b)** S-G filtered data using an interval of 11 data points and a polynomial of the first degree.

Extracting Relevant Parameters from Hysteresis Curves

The saturation magnetization, M_S, was found by averaging the highest and the absolute value of the lowest magnetization value from the filtered hysteresis. M_S can be expressed mathematically as

$$M_S = \frac{|m_{\min}| + m_{\max}}{2 \cdot V_{\text{sample}}} \quad \left[\frac{\text{emu}}{\text{cm}^2}\right]. \tag{3.2}$$

The coercive field, H_C, is calculated by averaging the absolute value of the field size at the first interception of the x-axis and the field size at the second interception of the x-axis.

$$H_C = \frac{|H\,(m=0)_1| + H\,(m=0)_2}{2} \quad [\text{Oe}] \tag{3.3}$$

By averaging both sides, experimental errors related to shifts where the center of the hysteresis does not align with the origin are corrected.

The sharpness of the hysteresis loops is of interest when assessing the mechanisms behind the coercive field. However, a quantitative measure of the sharpness is required to compare the hysteresis curves other than by visual inspection. In the absence of a conventional way to provide a quantitative description of the sharpness of the jump in the hysteresis loop, the method described in Figure 3.6 to find the *switching length* was established. The right half of the hysteresis curves were numerically differentiated by the central difference method on the form

$$M'(H_i) = (M(H_{i+1}) - M(H_{i-1})) \cdot (H_{i+1} - H_{i-1})\,. \tag{3.4}$$

After obtaining the differentiated hysteresis curves, a Gaussian fit was applied to the differentiated curve. Using the standard deviation (σ) from the resulting gaussian as a quantitative measurement for the sharpness in jump after domain wall nucleation has taken place in the hysteresis curves. A minor standard deviation corresponds to a sharper jump in the hysteresis curve, meaning domain wall motion needs less energy. The parameter that will be called the switching length is defined as four times the standard deviation. This interval covers 95.45 % of the area under the Gauss fit and serves as a reasonable estimate for the broadness of the jump.

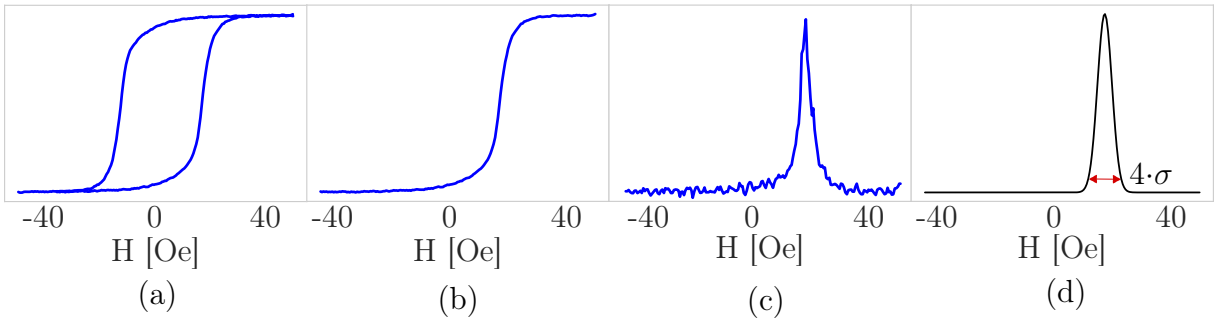

Figure 3.6: Obtaining quantitative measurement for the sharpness of the hysteresis loop | **(a)** S-G filtered hysteresis profile. **(b)** The left half of the hysteresis is removed. **(c)** The right half of the hysteresis profile is differentiated using Equation (3.4). **(d)** A Gaussian fit is applied to the differentiated hysteresis curve. By extracting the standard deviation from the Gaussian fit, we define the switching length as four times the standard deviation. Thereby, a quantitative measurement of the sharpness is obtained.

Chapter 4

Results and Discussion

This chapter will present and discuss the results of the studies of magnetic thin films on rough substrates. The first section contains results from studies of gold thin films by E-beam evaporation. The following section will present a thorough investigation of the Cu thin films and discussions of their properties. The third and last section contains results from the studies of magnetic thin films on substrates of different Cu thicknesses. The analysis of hysteresis curves obtained by VSM measurements will be linked to the surface topography of the substrate.

4.1 Gold Surfaces as Striplines

Au is a good candidate for metallic striplines because of its high conductivity and resistance to oxidation [47, 48]. These qualities are essential for creating a reliable and easily controllable field for the artificial spin ice. Au thin films were, therefore, initially a necessary subject for this thesis. 150 nm thick films have been prepared by e-beam evaporation. The surface characteristics vary depending on what rate Au is deposited. Figure 4.1 displays AFM scans of four different samples of Au thin films deposited at rates of 1, 3, 5, and 7 Å/s. Table 4.1 displays the rms roughness of each deposited Au layer. It can be seen that the lowest deposition rate produces the highest surface roughness. Increasing rms roughness when lowering the Au evaporation rates ≤ 1 Å/s have been reported in a different study [49]. The behavior is reportedly caused clustering of Au droplets at the surface when decreasing the evaporation rate (and thus increasing evaporation time). The clustering of Au causes larger grains to form, thereby raising the rms roughness of the substrate.

In order to confirm if the change in roughness parameters is related to the clustering of Au droplets into larger grains, grain sizes were obtained by applying watershed segmentation on the AFM images. The results are presented in table 4.1 along with the standard deviation of each grain size. As expected, Au evaporated at lower evaporation rates tends

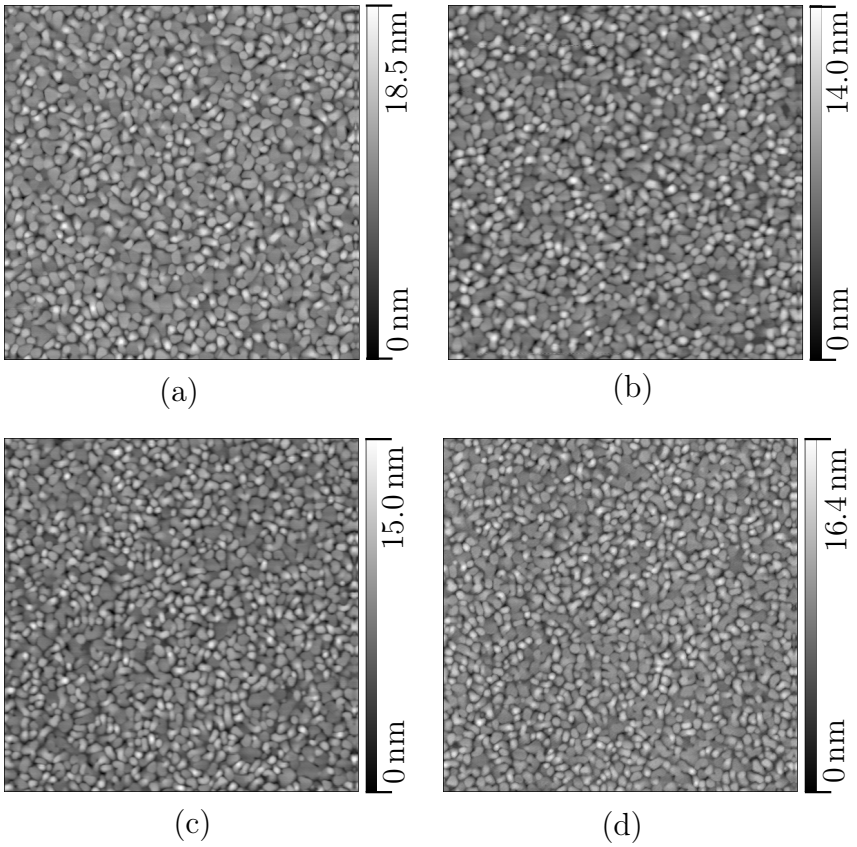

Figure 4.1: Atomic force microscope (AFM) images of 150 nm thick Au thin films | AFM images are acquired by scanning a 2x2 μm^2 area. The thin films has been deposited using an Au evaporation rate of **(a)** 1 Å/s **(b)** 3 Å/s **(c)** 5 Å/s **(d)** 7 Å/s

to form larger grains when the material cools down on the sample surface, although the differences are not significant. An evaporation rate of 1 Å/s results in an average grain size of $d = 66.6$ nm while an evaporation rate of 7 Å/s has an average of $d = 59.1$ nm. The clustering of Au into more spherical particles for 1 Å/s could be the reason for the high rms roughness. The evaporation rate of 3 Å/s has evidently the lowest rms roughness and is thereby the best suited choice.

4.1.1 Spitting

Although it has been clarified that elevated Au evaporation rates (≥ 3 Å/s) inherit lower surface roughness and smaller grain sizes, a different problem emerges for these rates, *spitting*. By visual investigation of the images captured with a light microscope in Figure 4.2 it is evident that both the size and amount of Au particles escalate when evaporation rates increase. The amount of liquid droplets escaping the Au target depends on the process and material conditions. In this case, the material conditions can be assumed equal since the target has not been changed between the depositions. As for the process

Table 4.1: Average grain sizes, d, with standard deviation for 150 nm Au thin films deposited at different evaporation rates. The grain size, d, is the diameter of a circle with the same area as the grain and is calculated by the equation $d = \sqrt{4A/\pi}$ where A is the projected area of the grain.

Au evaporation rate	rms roughness [nm]	Avg grain size, d [nm]	Std [nm]
1 Å/s	2.30	66.6	19.2
3 Å/s	1.98	64.4	19.2
5 Å/s	2.02	58.8	17.1
7 Å/s	1.99	59.1	17.5

parameters, the variable changing the deposition rate is the power input. More precisely, this is controlled and adjusted by manipulating the size of the electron beam current. Larger currents induce higher temperatures at the target, giving more vapor off the target surface. This is also causing a more significant amount of Au droplets to be emitted from the target. Spitting constitutes a problem when it comes to usage for IC applications as it can cause improper functioning. Gold thin films could still work for small nano-sized structures, depending on the density of Au particles on the surface. However, a fabricated stripline can be ruined if a liquid Au droplet is deposited on the structure during evaporation, rendering the sample useless.

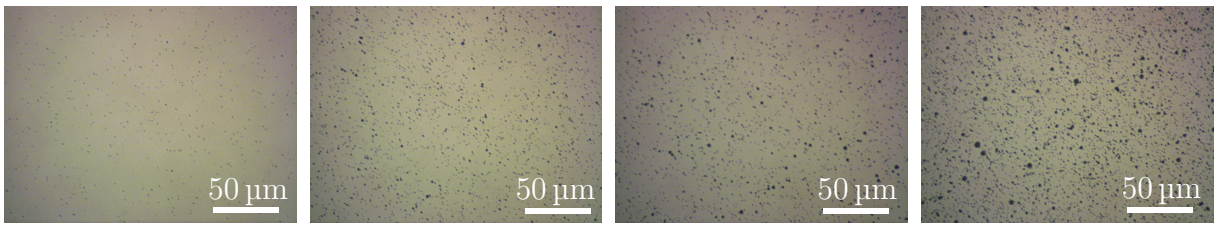

(a) (b) (c) (d)

Figure 4.2: Light microscope images of Au thin films deposited at different rates. | 150 nm thick Au thin films evaporated onto Si substrate at deposition rates of **(a)** 1 Å/s **(b)** 3 Å/s **(c)** 5 Å/s **(d)** 7 Å/s. The size and amount of contamination (Au particles) caused by spitting in the images are increasing at higher evaporation rates.

Investigation of the Au particles by Scanning Electron Microscopy (SEM) was performed. Figure 4.3 displays images from the thin film with a deposition rate of 7 Å/s which was most prone to spitting. Au nanoparticles of sizes up to 1 µm have been deposited at different sites on the thin film. The images reveal the underlying Au surface morphology, which was characterized using AFM.

An interesting detail is the facet development on the surface of the Au particles. The most stable morphology for nanoparticles can be predicted through surface energy minimization. For gold particles larger than a few nanometres, this is calculated to be a truncated

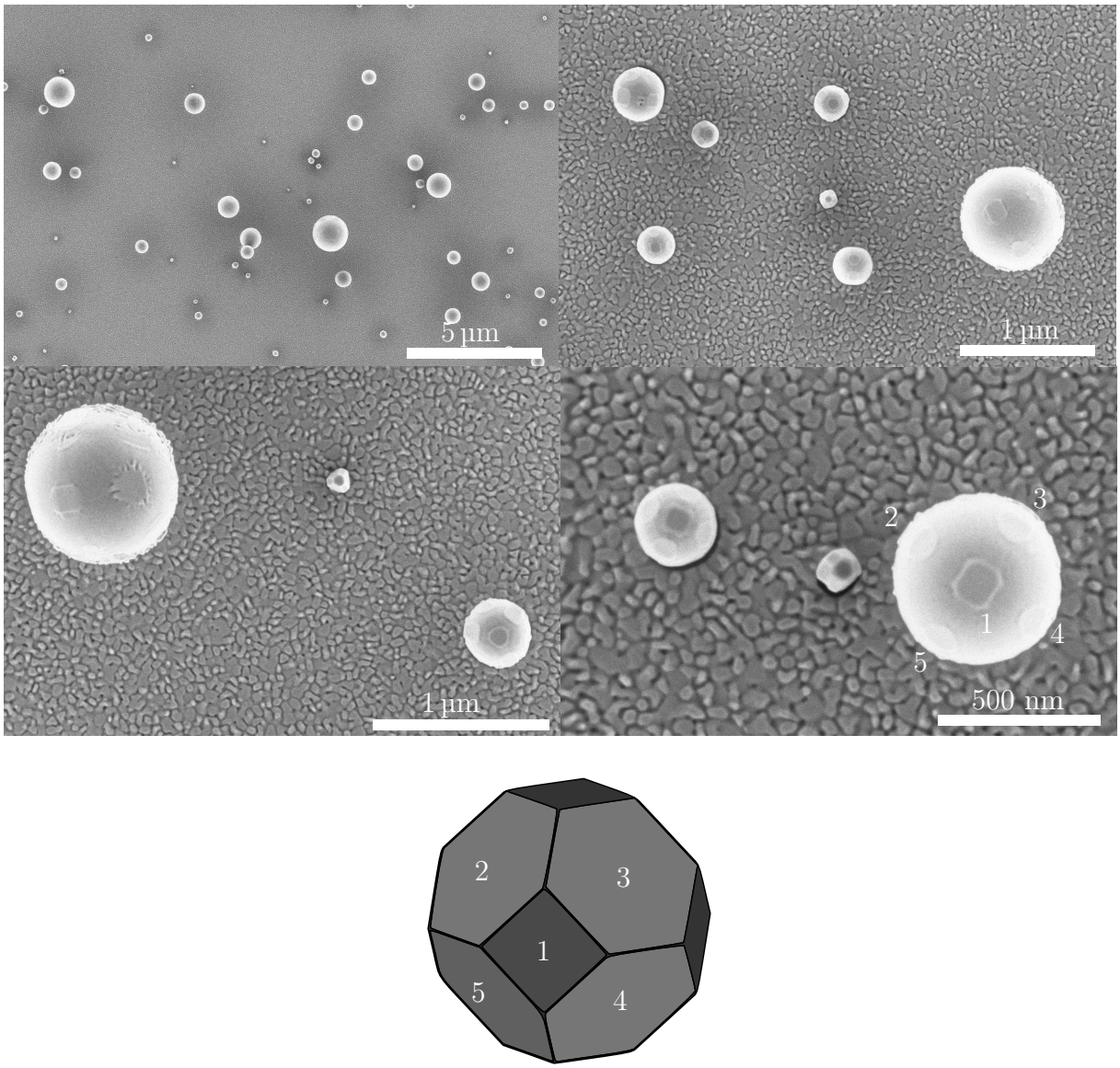

Figure 4.3: Top: High-resolution Scanning Electron Microscope (SEM) images of Au particles on Au thin film. Bottom: Drawing of the Wolff shape | Images are obtained for the 150 nm thick Au thin film deposited at 7 Å/s. The Au particles caused by spitting are attached to the surface. The diameter of the particles are ranging from below 100 nm up to 1 µm. The facets of one of the nanoparticles are numbered in correspondence to the drawing of the Wolff shape. The same shape can be found in all the particles.

octahedron, or the Wolff shape [50, 51]. The shape can be seen in Figure 4.3. The truncated octahedron can be imagined as an octahedron with the corners cut off. The shape is most prominent in the smallest particles. Most of the particles in the image are so large that they have almost formed spheres, however, the facets from the Wolff shape are still visible. The shape is highlighted by numbering the facets of one of the particles.

4.2 Surface Roughness Profiling of Cu Substrates

When reading this and the next section, keep in mind that when referring to the 150 nm Cu thin film, the actual sample consists of a 5 nm Ti layer deposited before and a 5 nm Al layer deposited after deposition of a 140 nm Cu layer. This goes for the 100 nm and 50 nm Cu thin films as well. The exception is the 0 nm Cu (just the Si wafer).

4.2.1 Cu Surfaces Profiles

Before lithography was performed on samples containing layers of 150 nm, 100 nm, 50 nm, and 0 nm of Cu, an assessment of the surfaces was performed using the data gathered with the atomic force microscope (AFM). The aim was to extract relevant parameters that can be used to interpret dissimilarities in the hysteresis curves after Py films are fabricated on the surfaces.

Figure 4.4 shows the 3D topography of our substrates where the relative scaling of the z-direction is 1:1 between the sub-figures. From visually examining these substrates, it is noticeable that the character of the surfaces is quite similar. The most noticeable difference is the height and size of the peaks and valleys, which will impact the substrates' roughness values. In addition, the grain sizes are different in the four substrates.

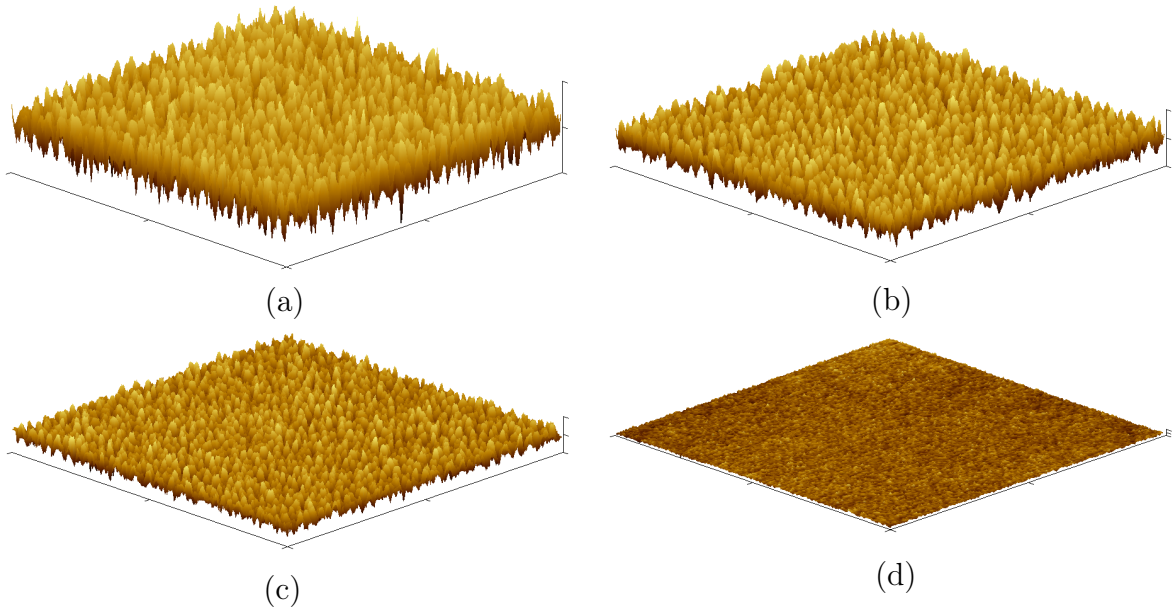

Figure 4.4: AFM images of all four surfaces after Cu deposition on Si wafers. | The axes are scaled 1:1 with each other for better comparison. The scan areas are 2×2 µm in the x- and y-dimension. The thickness of the metal layers and the size of the z-scalebars are: **(a)** 150 nm Cu. z-scalebar: 18.3 nm. **(b)** 100 nm Cu. z-scalebar: 11.3 nm. **(c)** 50 nm Cu. z-scalebar: 7.2 nm. **(d)** 0 nm Cu. z-scalebar: 1.2 nm.

All four Cu thin films used in this study have different surface roughness values. The manufacturer of the Si substrates does not report an rms roughness for the wafer surface. From the AFM scans obtained at nanolab, the rms roughness of the silicon wafer is measured to 128 pm. The average rms roughness measured for the other surfaces are 0.97 nm for 50 nm Cu, 1.63 nm for 100 nm Cu, and 2.31 nm for 150 nm Cu. Figure 4.5 displays three different scatter plots displaying surface characteristics for the four substrates. The rms roughness and arithmetic mean roughness display a close to linear behavior. The linearity has been highlighted by performing a linear fit using the least squares method. The resulting estimate for rms and arithmetic average (S_a) for a given thin film thickness, x [nm], is then given as:

$$\mathrm{rms} = 0.0144x + 0.176 \quad [\mathrm{nm}] \tag{4.1a}$$

$$S_\mathrm{a} = 0.0119x + 0.142 \quad [\mathrm{nm}] \tag{4.1b}$$

It should be noted that the equations in 4.1 are instrument and parameter specific. The thin films were grown on the E-beam evaporator and sputter AJA at deposition rates of 5 Å/s using an automatic process.

The roughness parameters excess kurtosis and skewness are displayed in respectively Figure 4.5b and 4.5c. The Si surface is close to uniform, approaching the resolution limit of the AFM tips. Therefore, the corresponding roughness values deviate slightly from zero. The excess kurtosis is negative for all surfaces except the clean Si wafer, meaning that the grains are more bumpy or flat rather than spiky. A spiky surface would suggest sharp peaks and valleys on the grains. The 100 nm thick Cu thin film stands out from the rest, having an average excess kurtosis of -0.60, whereas the corresponding average values for 50 nm and 150 nm thick Cu films are -0.41 and -0.42. This difference can have an impact on the magnetic thin film properties.

Assessment of Measurement Variations

For each surface, three AFM scans have been performed at randomly chosen locations at the wafer. Because the measurements have been performed at different locations, it is essential to look at variations in the results. Nevertheless, the results seem reliable, given that the sample-to-sample variations are more significant than the variations in the scans performed on each sample. With this, we can safely assume that the variations across the wafer are minor and that our measurements provide the correct information.

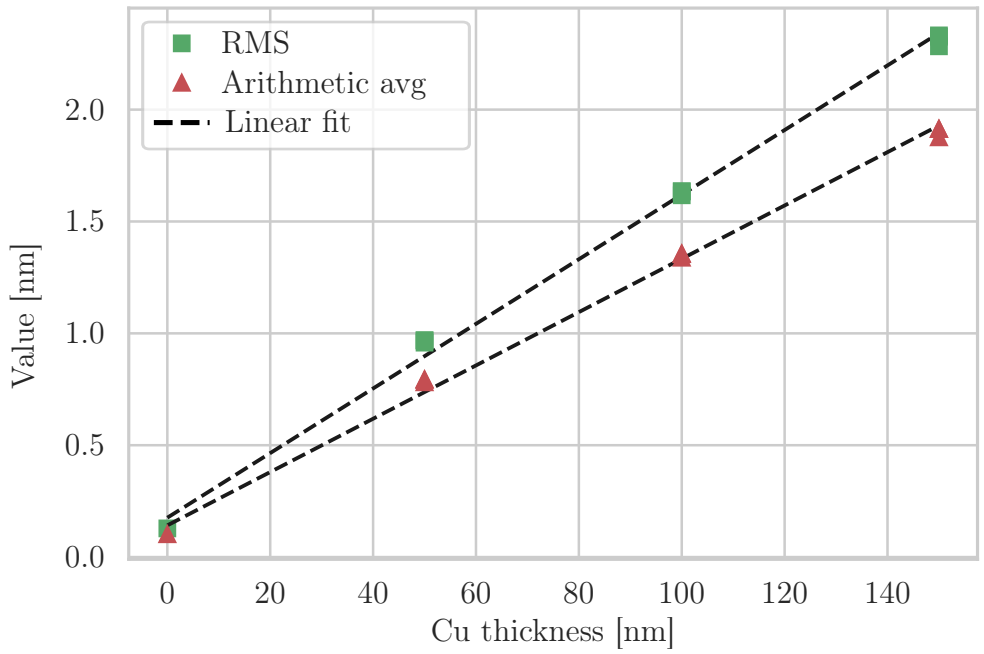

(a) RMS and Arithmetic average

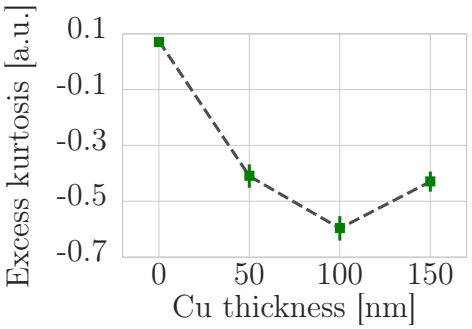

(b) Excess kurtosis

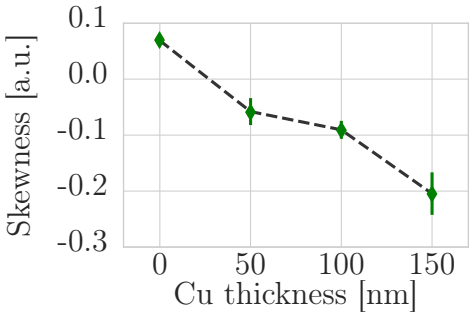

(c) Skewness

Figure 4.5: Overview of roughness parameters for the four different Cu thin films | The x-axis display the thickness of the respective Cu layers. **(a)** The rms value and arithmetic average. Linear fits using the method of least squares are applied. **(b)** The excess kurtosis was found to have a lower value for 100 nm Cu. **(c)** Skewness decreases with the film thickness.

4.2.2 Grain Size Distributions

The distribution of grain diameters, or "mountains", are displayed in Figure 4.6 for the Cu surfaces and constitute the wavelength of the wavy-like surface of the Ti/Cu/Al metal layers, or the lateral size of each mountain. Each bar of the histograms represents the density of grains corresponding to the grain diameter. Each histogram has a superimposed curve fitted Gaussian function, and the expectation values and standard deviations are displayed in Table 4.2. As expected, both the average grain size and the standard deviation of grain sizes are increasing with the thickness of the Cu thin film. The 50 nm thick Cu thin films has an average grain size of 44.56 nm whereas the 100 nm and 150 nm Cu thin films have average grain sizes of respectively 56.80 nm and 63.33 nm.

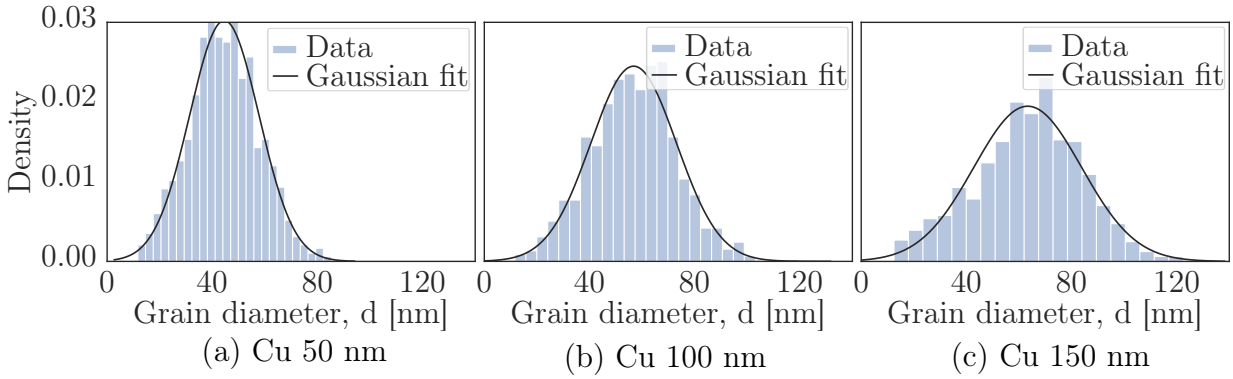

Figure 4.6: Density of grain sizes with fitted Gaussian function | Histograms display density of occurrences vs grain diameter, d, for **(a)** 50 nm, **(b)** 100 nm, and **(c)** 150 nm Cu thin films. The data is obtained using a watershed algorithm in Gwyddion applied to the .spm data gathered with the AFM. A Gaussian fit function has been used to describe the distribution of grains.

The grains' length is important for permalloy thin films for several reasons. Firstly, the grain diameter can be said to constitute the size of the surface inhomogeneities. When these inhomogeneities are larger than the typical width of the permalloy domain walls, this can cause the domain wall pinning. This mechanism affects the shape of the hysteresis loop because of a delay in the domain wall motion under the magnetization reversal process [17]. The domain wall motion is delayed when it intersects imperfections at local energy minima. The domain wall motion is delayed because the magnetization reversal process requires a larger field size when encountering the local minima, meaning an increased coercive field strength in the hysteresis curve. Trunk et al. [52] studied the domain wall structures of permalloy thin films for different thicknesses of Py. The simulation performed in the study showed that the domain wall undergoes a Bloch to Nèel transition for a Py thickness between 30-35 nm. Below the transition thickness, the Nèel wall was found to be energetically favorable, and the width of the domain wall increased linearly when reducing the Py thickness. A domain wall width of 34 nm was reported for Py thickness of 35 nm, and a domain wall width of 91 nm was reported for a Py thickness of 10 nm. Using this information about Néel walls in Py thin films, we can assume that the width of a typical

Néel wall in 20 nm Py is in the range between 34 nm and 91 nm. Therefore, the domain wall width is comparable to the grain size distributions in the Cu thin films, meaning pinning of domain walls are highly relevant.

Table 4.2: Curve fit parameters obtained for the Gaussian functions in Figure 4.6. The important parameters are the mean value, μ, and the standard deviation, σ. The size and the standard deviation of the grains are increasing for escalating values of film thickness.

Sample	Mean value [nm]	Standard deviation [nm]
50 nm Cu	44.56	13.21
100 nm Cu	56.80	16.29
150 nm Cu	63.33	20.50

Py Surface Structure

Typically, the morphology of the substrate will act as a template for Py or Fe thin films [17, 53, 54]. Therefore, it is doubtful that the 20 nm Py and 2.5 nm Al layers will introduce an entirely new surface structure based on the thickness of the layers. In order to verify if the surface structure of the substrate would be transferred to the Py layer, high-resolution SEM images were captured at the edges of the Py disc. These images are presented in Figure 4.7. As shown, the Py thin film replicates the underlying substrate.

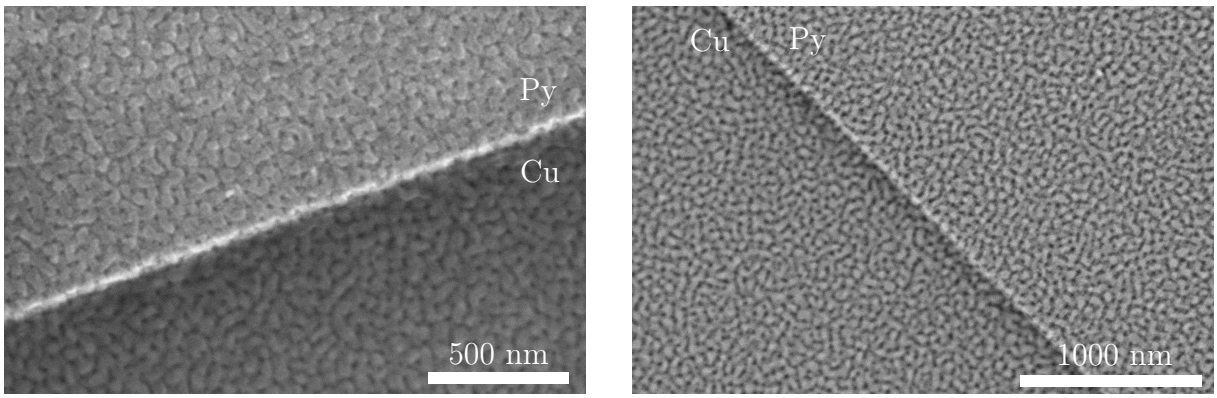

(a) (b)

Figure 4.7: SEM micrographs of Py thin film on Cu substrate | The images display the edge of the Py disc deposited on 150 nm Cu substrate. The surface structure of the substrate has been transferred to the Py thin film. The SEM images where obtained using **(a)** T2 detector and **(b)** T1 detector.

4.3 Magnetic Properties of Py Thin Films

Hysteresis curves from Py discs fabricated on four substrates were obtained using VSM. Figure 4.8 display the S-G filtered hysteresis curve of one Py sample for each of the four substrates. In total, three samples from each of the four substrates were measured. All samples were measured at one angle, then rotated 90° and measured again. Figure 4.9 displays all the obtained hysteresis curves with an applied S-G filter. The measurement range in the applied field was adjusted concerning the coercive field of the sample in order to obtain the complete hysteresis loop. A measurement range of $H \in [-20, 20]$ Oe was used for Py discs fabricated on a flat surface (Si wafer), $H \in [-40, 40]$ Oe for Py discs on the 50 nm and 100 nm Cu substrate, and $H \in [-50, 50]$ Oe for the Py discs on the 150 nm Cu substrate. All measurements were performed at room temperature.

The appearance of the hysteresis curves in Figure 4.9 are typical for Py thin films. The curves generally have slight, expected sample-to-sample variation, but some exceptions should be mentioned. The first is the anisotropy observed in Figure 4.9a. The magnetic behaviour of the Py film deposited directly on Si depends on the direction of the applied field. The directional dependence is not observed for Py on Cu substrates. The second is the contrast in the behavior in one of the Py thin films deposited on 150 nm Cu as shown in Figure 4.9d. The variance of the coercive field is generally low for most Py films. However, one of the 150 nm Cu samples seems to deviate from the rest. The explanation for this discrepancy are unknown.

The anisotropy in Py thin films deposited on the Si substrate is strange, as we do not see the same effect on the Cu substrates. On the contrary, findings in other studies have shown no anisotropy in Py deposited on Si substrates. Instead, surface-induced anisotropy when introducing a directional or non-directional surface roughness was observed [54, 55]. Based on the result presented in Figure 4.9, we can not conclude that there is no anisotropy in the Cu substrates. This is because we have only applied an external field along two axes perpendicular to each other. If both axes lie between an easy axis and a hard axis, it is hard to detect any anisotropy. Variation in magnetic anisotropy can be characterized by measuring the magnetization along the whole 360° circle with smaller step sizes. Such measurements are typically performed by magneto-optical Kerr effect (MOKE) measurements [56]. However, with the setup used in this thesis, such measurements were not possible. Therefore, it is hard to conclude why this behavior is observed, and further investigations are needed. Possible reasons for the observed anisotropy could be field-induced-magnetic-anisotropy if a magnetic field influences Py during deposition or vsm initialization [57]. Another possible reason could be an antiferromagnetic/ferromagnetic coupling between the antiferromagnetic oxidized Py and the ferromagnetic Py layer. Antiferromagnetic/ferromagnetic coupling can occur if the thickness of the oxidized Py is sufficient to pin the ferromagnetic layer [28].

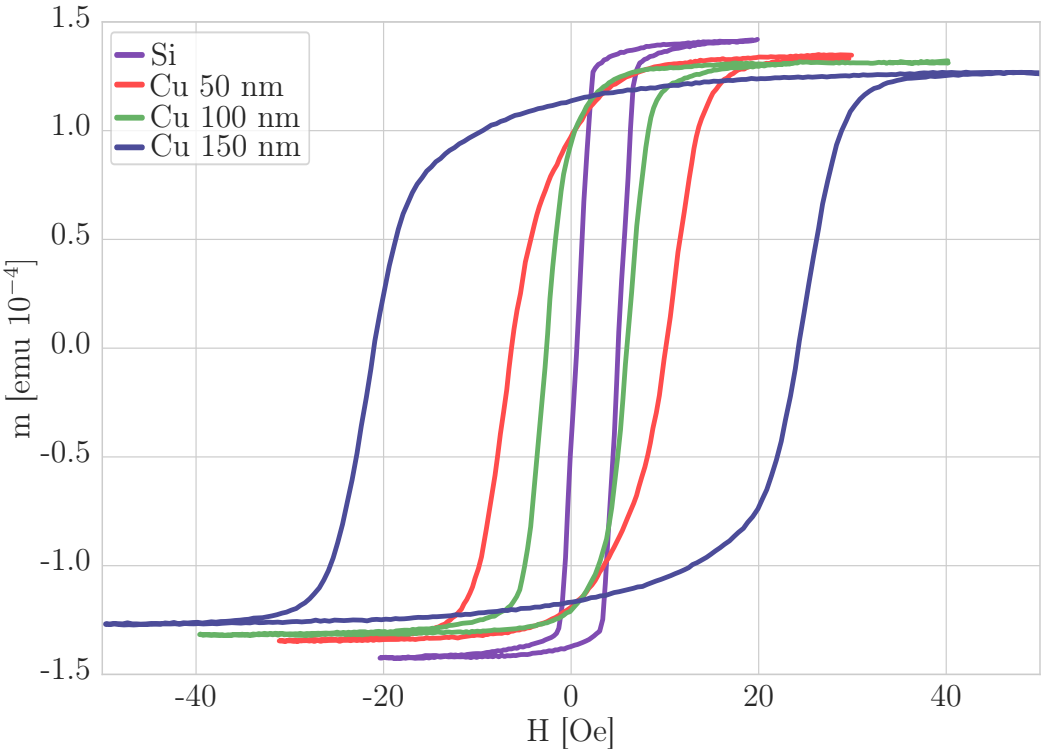

Figure 4.8: Hysteresis curves for 20 nm Py discs fabricated on different substrates | The legends display what substrate the Py discs were deposited on. The Py discs were fabricated with a 2.5 nm capping layer of Al. The figure displays one out of the six measurements from each batch to portray the differences between the hysteresis curves.

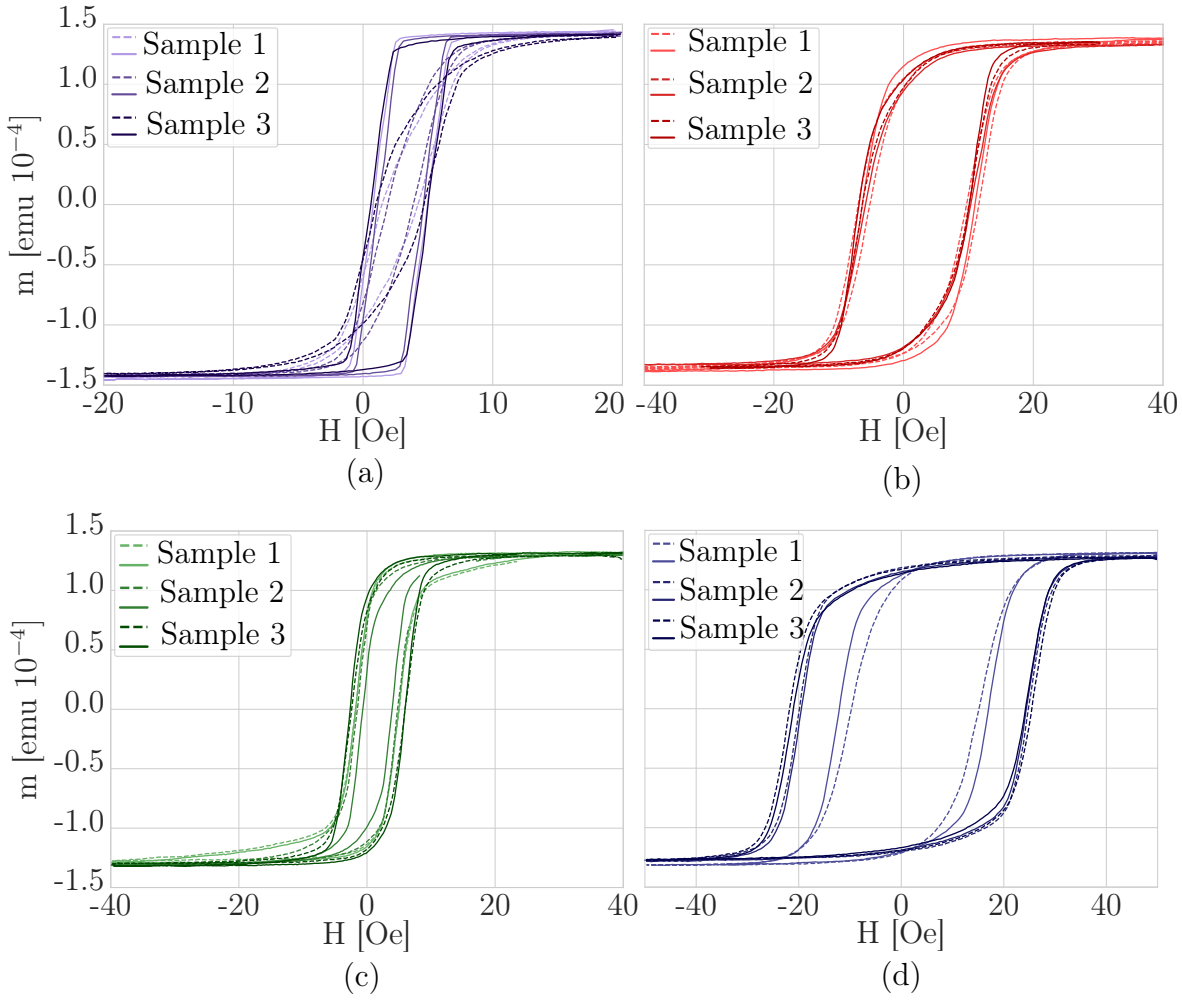

Figure 4.9: S-G filtered hysteresis curves for 20 nm Py discs with 2.5 nm Al capping fabricated on four different substrates | The graphs display hysteresis curves obtained from circular Py discs fabricated on **(a)** 0 nm Cu, **(b)** 50 nm Cu, **(c)** 100 nm Cu, and **(d)** 150 nm Cu substrate. Three samples from each batch were measured with the VSM. Each sample was measured at a certain angle, then rotated 90° and measured again. Small sample to sample variations can be observed for each substrate. There are two noticeable variations in the shape of the hysteresis loops for "identical" samples. The first one is the anisotropy observed for Py fabricated directly on Si (0 nm Cu). The second one is the difference in the coercive field of Py discs fabricated on 150 nm Cu. Shifts along the x-axis are caused by instrumental errors and not intrinsic properties of the material.

4.3.1 Roughness Effects on Saturated Moment and Coercive Field

The coercive field and saturated magnetic moment were extracted from the filtered hysteresis curves and plotted against the rms roughness of the substrate in Figure 4.10. As seen in the previous section, the rms roughness increase with the thickness of the deposited metal layer. In other words, the largest rms value corresponds to the Py discs fabricated on a 150 nm Cu substrate, while the smallest corresponds to the Si substrate with no metal layers underneath the Py discs. The saturated magnetic moment shows a trend of a reduced moment as the substrate rms value increases. Py deposited directly on the Si wafer (rms = 0.128 nm) measures a saturated moment of $M_S = 744$ emu/cm^3, while the same film deposited on 150 Cu with a roughness value of rms = 2.31 nm has a moment of $M_S = 671$ emu/cm^3. The corresponding loss of magnetic moment is 9.8 %.

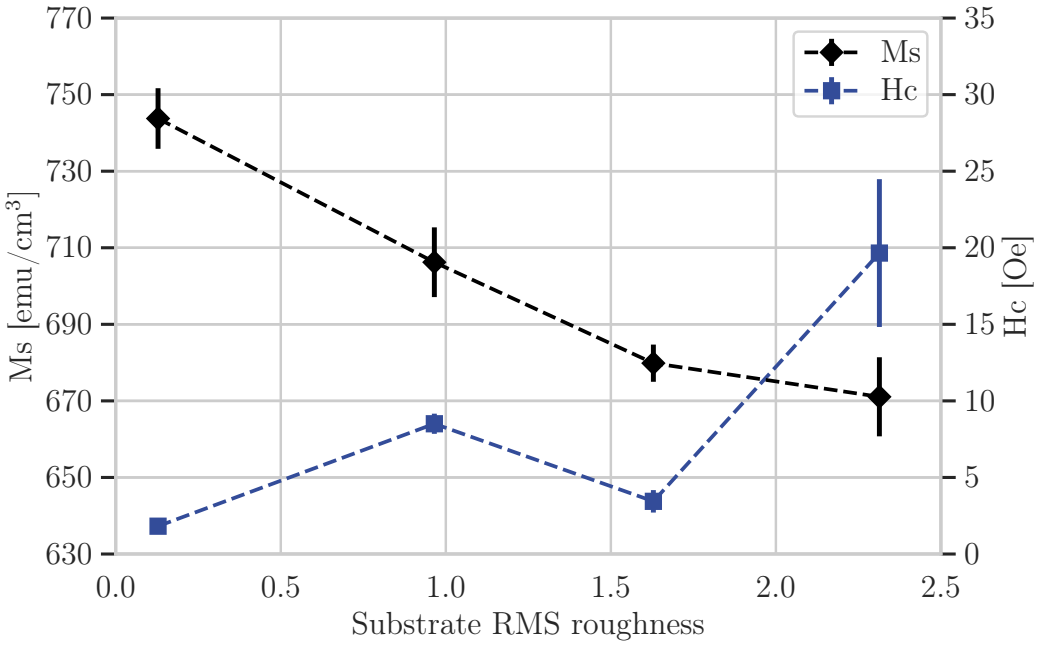

Figure 4.10: Saturated magnetic moment and coercive field strength versus substrate roughness | The plot is based on the S-G filtered experimental data from Figure 4.9. Three different samples from each batch and two measurements of each sample (0° and 90°) were performed. The error bars indicate the standard deviation. The saturated magnetic moment, M_S, is calculated by using the volume of the Py discs with $d = 3.5$ mm and $t = 20$ nm.

The tendency of a dropping saturated magnetic moment as the thickness of the Cu layer increases is striking. A close to 10 % loss of magnetic moment is significant, and the (almost) linear tendency suggests that the surface roughness of the substrate influences the saturation magnetization. One possible source of loss in the saturated magnetic moment could be the oxidation of Py. As the surface roughness increases, the total surface area

increases. Table 4.3 displays the total surface area of the four substrates based on AFM data from a 2 µm×2 µm scan area. An increased surface area means a larger area potentially affected by oxidation. A 2.5 nm capping layer of Al is deposited on top of the Py layer. As presented in the previous section, the rms values range to 2.1 nm, comparable to the Al thickness. Since e-beam evaporation is a directional technique, the Al layer is deposited perpendicular to the sample surface. Because of the substrate's surface roughness, some surface parts are less covered than others, making them more exposed and prone to oxidation. Therefore, it is not unlikely that the drop in saturation magnetization is a direct consequence of Py oxidation.

Table 4.3: The total surface area of Cu thin films of varying thickness deposited on Si substrate, obtained by AFM measurements. The surface areas have a projected area of 4.000 µm^2.

Sample	Total surface area [µm^2]
0 nm Cu	4.001
50 nm Cu	4.058
100 nm Cu	4.092
150 nm Cu	4.189

Another possible reason for the drop in saturation magnetization is the diamagnetic response of Cu. However, the diamagnetic response of Cu is small and should be independent of the thickness of the Cu layer. Nevertheless, the loss of momentum from the diamagnetic response can be calculated. The susceptibility of copper is $\chi_{\text{Cu}} = -1 \cdot 10^{-5}$ [58]. Using Equation (2.5) with an applied field size of 50 Oe we get $M_{\text{dia}} = 39.8 \cdot 10^{-6}$ emu/cm^3, which is microscopically small compared to the observed losses.

We can compare the obtained saturation magnetizations with values from the literature. Zhang et al. [59] have performed a detailed study of the magnetization of Py thin films with varying thickness and temperature. Using the magnetization versus temperature graph for 20 nm Py thin films presented in the supplementary information, an estimate of the saturation magnetization was made. Since the temperature range in the study varied from 400 K to 800 K, a curve fit on the form $f(T) = -a \cdot \log(-b/(T-c))$ was applied to find the value at room temperature. Data points corresponding to the magnetization curve were obtained using webplotdigitizer [60], and the curve fit was found using the curve_fit function from scipy [45]. Appendix A includes the originalø figure, extracted data points, and obtained curve fit. The resulting curve fit parameters were $a = 242.72$, $b = 16.99$, and $c = 841.65$, with standard errors of $\text{SE}_a = 3.57$, $\text{SE}_b = 0.78$, and $\text{SE}_c = 1.53$. Finally, the magnetization at 300 K was estimated to 840.2 emu/cm^3. The measured saturation magnetization for our 20 nm thick Py thin film was 744 emu/cm^3, which lower than the magnetization found in the literature. There could be several reasons why the measured magnetization is lower than the values from the literature. Small offsets in the area of the disks, calibration of rate monitors in the EBE, and oxidation effects in the exposed disc

edges can be reasons why the magnetization is lower. However, these contributions will not affect the results of this thesis as all samples are affected equally.

The effect of surface roughness on the coercive field is visible in Figure 4.10. The size of the coercive field has drastically increased for the Py thin films on 50 nm and 150 nm Cu substrates. However, despite an increase in surface roughness, the 100 nm Cu samples show deviation from the trend of increasing coercive field. This rather contradictory result suggests that the mechanisms that delay the magnetization reversal process are somehow put out of play. It is hard to conclude why the coercive field displays such unpredictable behavior. However, suppose we assume that the substrates' surface structure controls the coercive field strength. In that case, a possible explanation could be the shape of the grain or, more specifically, the parameter called excess kurtosis. The excess kurtosis is the only surface roughness parameter that did not show a correlation to the thickness of the Cu film. As previously mentioned, the 100 nm Cu film has a lower excess kurtosis, meaning that the grain peaks, in general, are more *bumpy*. Therefore, it could be suggested that the energy barrier created by domain wall pinning is lowered because sharp peaks or valleys are not present to delay the in-plane Neel wall propagation. The remaining question is if the difference in excess kurtosis between -0.4 and -0.6 could significantly impact the domain wall pinning. It should also be noted that all Cu surfaces can be characterized as bumpy, as the excess kurtosises are less than 0.

4.3.2 Domain Wall Dynamics

For ideal materials, which are perfect in geometrical shape and phase composition, Coherent rotation and curling are the primary mechanisms for coercivity. However, in the real world, such conditions are rarely fulfilled. In experimental work, we are forced to deal with imperfections and dislocations, especially in this case when working with rough substrates for our Py thin films. Therefore, the primary mechanisms for coercivity are domain wall pinning, and nucleation [61]. Because the initialization process ran before the measurements in the VSM Versalab system, the sample was already saturated before obtaining hysteresis curves. Therefore the virgin magnetization curve was not obtained. The virgin magnetization curve is only affected by domain wall pinning, as domain walls already exist in the ferromagnet's initial state. Therefore, the virgin magnetization curve could have provided information about the domain wall motion in the thin film. However, the coercivity mechanisms also affect the shape of the hysteresis loop in other ways, making it possible to identify the dominant mechanisms for varying substrates.

In this subsection, we are taking a closer look at the two hysteresis loop characteristics, squareness and switching length. A large squareness (M_R/M_S) often indicates magnetic reversal limited by domain wall nucleation, while magnetic reversal limited by domain wall pinning causes a less sharp jump in the hysteresis loop after domain wall nucleation takes place. The less sharp jump is observed because the inhomogeneities in the film inhibit the domain wall motion, causing a stepwise movement of the domain walls [17]. The results

for Py thin film on Cu substrates will be presented and discussed first before we look at Py deposited directly on Si.

The squareness is plotted versus the coercive field in Figure 4.11a. The squarenesses are respectively 0.79, 0.84, and 0.91 for Cu thicknesses of 100 nm, 50 nm, and 150 nm. At first glance, one can assume that the coercive field is determined by the delay in domain wall nucleation since the squareness increases with the coercive field. However, a squareness value closer to 1 was expected for domain wall nucleation to be the limiting mechanism for the increased coercivity. A squareness of 0.91 indicates that the remanent field has decreased by 9 % when the applied field is zero. At this point, the domain wall nucleation has already happened, and domain wall motion is initiated. The fact that domain wall pinning is more influential than domain wall nucleation is also indicated by the trend in squareness for Py thin films on Cu substrates. The squareness increases with an increasing coercive field, indicating that the domain wall energy landscape generally is more characterized by higher pinning energy barriers. The domain wall motion is in the creep regime at zero applied field. The energy contributors in this regime are mainly the demagnetization field and depinning assisted by thermal fluctuations. A lower squareness indicates a faster movement of domain walls in the creep regime because of lower domain wall pinning energies.

The sharpness of the jump in the hysteresis loop can be described through the switching length. Figure 4.11b shows the switching length plotted against the coercive field for Py discs on different substrates. The switching length increases for increasing coercive field, indicating that the delay in domain wall motion plays a prominent role in the magnetization reversal as the jump in the hysteresis loop is less sharp. A fascinating observation is that the domain wall pinning appears to be much less prominent in the 100 nm Cu film, although it has a larger rms roughness than the 50 nm Cu film. As discussed in the previous section, the critical difference between the Cu morphologies is the excess kurtosis, indicating that the grains are bumpier rather than spiky on the 100 nm Cu surface. A possible explanation to these results could be that the energy barriers created by domain wall pinning are significantly lowered for grains with a more bumpy-like nature. However, simulations of such barriers or further experimental research are needed to conclude that the excess kurtosis is the main reason for the reduced domain wall pinning and coercivity for Cu substrates.

A more direct way of observing the domain wall pinning is through the Barkhausen effect in the unfiltered hysteresis loops. However, the measurement noise overrides the effect rendering the reliability of observations resembling the Barkhausen effect. Additionally, even shorter applied field steps and more precise measurements are needed to observe the effect. The sample is sizable, and pinning cites exists all across the disc. In addition, depinning assisted by thermal fluctuations at room temperature contributes to the smoothing of the hysteresis loop. The effect can also be observed by attaching the sensing coil to a loudspeaker. Crackling sounds, which can be compared to the unwrapping of candy, is then heard. This sound is called Barkhausen noise [15].

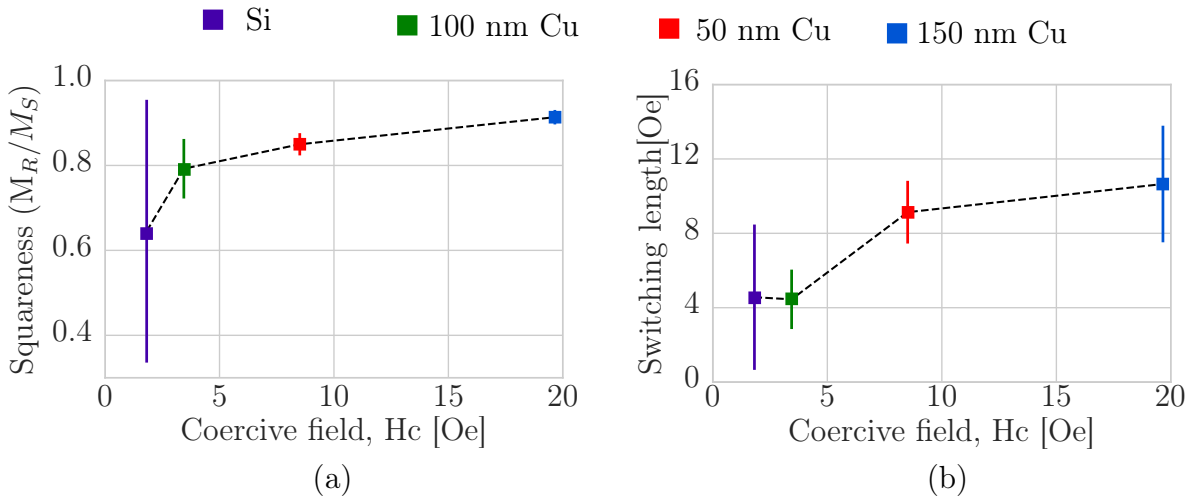

Figure 4.11: Squareness and switching length versus coercive field for 20 nm thick Py films with 2.5 nm Al capping on different substrates. | The labels display which substrate is used. **(a)** Squareness (M_R/M_S) versus coercive field. **(b)** Switching length versus the coercive field. The switching length is acquired by the method described in section 3.2.3. The switching length is four times the gaussian fit's standard deviation for differentiated hysteresis loops versus the coercive field.

As discussed in the previous section, Si is governed by a strong uniaxial anisotropy. Because the measurements are conducted along two axes perpendicular to each other, corresponding to the easy and hard axis, the measured hysteresis loops are of entirely different shapes. The anisotropy explains the significant standard deviation in Figure 4.11. The hysteresis along the easy axis is characterized by a large squareness (> 0.95) and a low switching length (< 1.5 Oe). The hard axis, on the other hand, is characterized by a low squareness (< 0.35) and a more considerable switching length (> 7.5 Oe). The switching energy is presumably driven by the energy landscape of the uniaxial anisotropy rather than the energy landscape shaped by domain wall pinning sites.

4.3.3 Roughness Induced Out of Plane Magnetization

In an ideal elongated nanomagnet used in ASI structures, the geometry is flat and uniform, and the magnetic moments point perfectly along the easy axis at zero applied field. Therefore, the demagnetization field is not strong enough to alter the nanomagnet's directional anisotropy. However, as we are dealing with rough substrates as a template for nanomagnets, the reality will be different. In this section, we will look at how the surface roughness from the metallic thin films will alter the magnetic moments inside nanomagnets.

For a Py thin film, the domain magnetization can have two possible magnetic configurations along a rippled structure. Figure 4.12 illustrates the two possible magnetic configurations. The Colombian approach is applied here to express magnetic moments as dipoles using positive and negative *magnetic charges*. In Figure 4.12a, surface charges are cre-

ated due to the corrugation of the film surface. These surface charges contribute to a $1/t$ thickness-dependent dipolar energy. The magnetic moments are aligned perpendicular to the surface in Figure 4.12b. When neighbor spins are not aligned, this will come at a cost governed by the exchange energy in addition to a small contribution of dipolar energy due to volume charges. Calculations aiming to find the energetically favorable configuration have been performed by Chen et al. [62]. For a ripple amplitude of 10 nm and an amplitude of 100 nm, the configuration of magnetic moments perpendicular to the surface was favorable for Co films with a thickness less than 150 nm. The Cu grains' length and height are comparable to these ripples, although the grains are slightly shorter and of lower amplitude. However, we assume here that the magnetic moments align perpendicular to the surface as our magnetic Py thin film is only 20 nm thick. When magnetic moments are aligned perpendicular to the surface, we can calculate the loss of magnetic moment due to in and out of the mean plane magnetization.

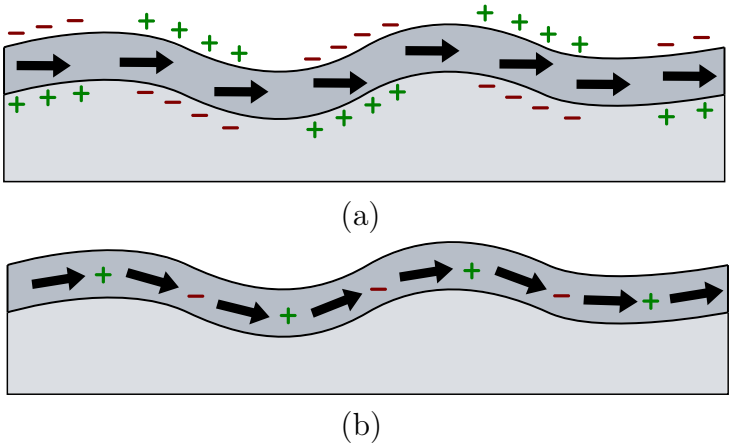

Figure 4.12: Sketch of two possible configurations for the saturated magnetization. | **(a)** The magnetization is pointing along the mean plane, surface charges, i.e., "sources" (green) and "drains" (red) of the magnetic field is created. These surface charges cause energy contributions in the form of magnetostatic energy. **(b)** The magnetization follows the surface structure. Adjacent magnetic moments deviate slightly, causing energy contributions from volume charges and exchange energy. This configuration is preferred for thinner films.

In order to calculate the total loss of magnetic moment along the "saturated" direction, the angle distribution for the angles in and out of the mean plane was obtained from the AFM data using Gwyddion. Figure 4.13 displays the distribution of angles in the direction in which the AFM scans were performed. Choosing the scan direction provides more reliable data (fewer scan errors), and since the substrate is spinning during deposition, there are no directional differences in the surface structure. The values are normalized so that the area's integral under the curves is equal to 1. Using the out-of-plane angle, β_i, and the density of angles, $\rho(\beta_i)$, we can calculate the loss of magnetic moment due to out-of-plane magnetization. β_i is the surface angle in lattice sites i compared to the mean plane in the

scan direction of the AFM tip. The fraction of magnetic moment that will align parallel to the mean plane, M_{mean}, is given by the cosine of the surface angle, β_i. When taking the normalization into account, we end up with the equation

$$M_{\text{mean}} = \frac{1}{\sum_{i=1}^{N} \rho\left(\beta_i\right)} \sum_{i=1}^{N} \rho\left(\beta_i\right) \cdot \cos\left(\beta_i\right). \tag{4.2}$$

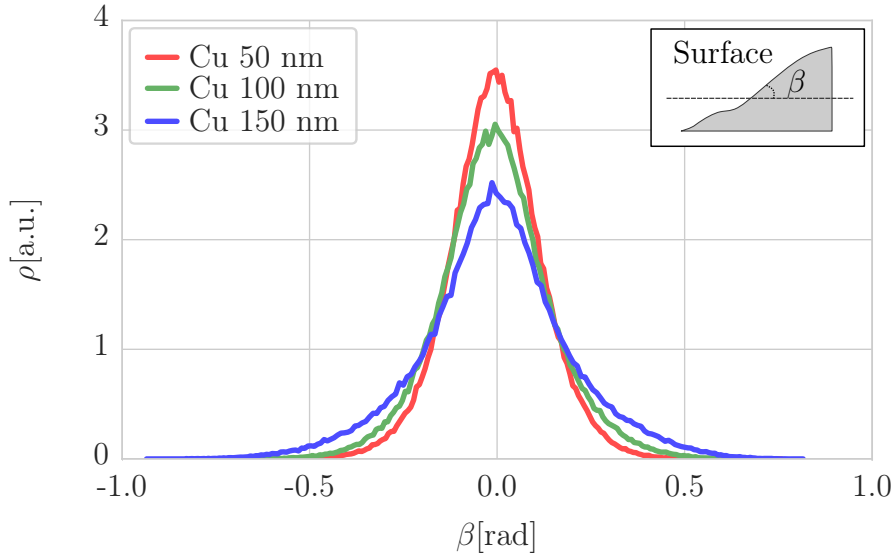

Figure 4.13: Angle distribution along the AFM scan direction (horizontal) | The inset shows how the angle β is defined at a given point on the surface compared to the mean plane. The graphs display the normalized density of β for 50 nm, 100 nm, and 150 nm Cu along the scan direction of the AFM tip. The normalization of the densities, ρ, is defined so that $\int_{-\infty}^{\infty} \rho\left(\beta\right) \mathrm{d}\beta = 1$.

The fraction of the vector length that will point along the macroscopic plane direction for Py thin films on each Cu substrate was computed. The respective results for substrates of 50 nm, 100 nm, and 150 nm Cu was 0.992, 0.988, and 0.978. In other words, there is a 2.2 % loss of magnetization along the mean plane axis of the 150 nm Cu substrate due to magnetic moments being oriented in and out of the mean plane. Elongated nanomagnets in ASI structures deposited on rough substrates are assumed to be influenced by this, thus altering the properties of the whole ASI structure. In addition to out-of-plane magnetization, in-plane deviation from the magnetization direction is expected. In other words, the effect can be expected to exceed the calculated loss of 2.2 %.

Unfortunately, the calculations can not be compared to the experimental results for our Py thin films. In the saturated region, we assume that the applied field is large enough to saturate the magnetic moments and have the configuration displayed in Figure 4.12a.

When the magnetization is turned off, the magnetic configuration in the domains is most likely parallel to the substrate's surface angle as in Figure 4.12b. However, in contradiction to mono-domain nanomagnets, the demagnetization field influences the orientations of moments inside the polydomain Py thin films. Therefore, both the orientation of individual domains and the out-of-plane magnetization contribute to the lowering of remanent magnetization.

4.3.4 Reproducibility of Results

This study investigates the surface characteristics of Cu thin films and the magnetic properties of Py thin films deposited on rough Cu surfaces. However, would we get the same results if we were to repeat the process? In order to investigate how accurate the obtained results are, the second batch of 50 nm Cu was produced with circle-shaped Py thin films using the exact procedure as before. Given the assumption that the surface morphology of the substrate governs the properties of the magnetic thin film, differences in the surface roughness parameters should be addressed first, and the changes in magnetic properties are discussed accordingly.

Table 4.4 displays relevant parameters obtained from surface roughness profiling and magnetic characterizations. The surface characteristics of the second batch are not a replica of the first batch. However, the changes are minor. The surface roughness is reduced from an rms of 0.965 nm to 0.911 nm, yielding a reduction of 5.6 %. The most pronounced percentile change is the 18.9 % increase in skewness. However, the skewness value is already so low that it cannot be perceived as a notable change. Furthermore, the excess kurtosis has increased from -0.409 to -0.352, which is quite formidable as it has been indicated that the grains' sharpness can significantly impact the domain wall pinning.

Table 4.4: Comparison of important surface roughness parameters for 50 nm Cu thin films from two different batches, and magnetic properties of 20 nm Py thin films with 2.5 nm Al capping deposited on top of the Cu layer. Note that the percentile change is calculated from the absolute value of each parameter.

Parameter	First batch	Second batch	Percentile change
Arithmetic average (R_A)	0.789 nm	0.743 nm	-5.8 %
Root mean square (rms)	0.965 nm	0.911 nm	-5.6 %
Skewness (S_{sk})	-0.058	-0.069	18.9 %
Excess kurtosis (S_{ku})	-0.409	-0.352	-13.9 %
Grain diameter (d)	44.6 nm	44.3 nm	-0.7 %
Grain standard deviation (d_{std})	13.2 nm	13.4 nm	1.5 %
Coercive field (H_C)	8.51 Oe	7.96 Oe	-6.5 %
Saturation magnetization (M_S)	707 emu/cm^2	671 emu/cm^2	-5.1 %
Squareness (M_R/M_S)	0.850	0.873	2.7 %

The coercive field and the saturation magnetization have approximately the exact percentile change as the root mean square and arithmetic average. The change in the coercive field complies with prior results. There has not been an increase in the excess kurtosis, and the roughness has just decreased a little However, the decrease in saturation magnetization was not expected based on prior results since the saturation magnetization tends to increase with decreasing roughness. The deviation can have several explanations, including a change of permalloy crucible in the Evaporator before deposition of Py in batch 2. It could also just be a batch-to-batch variation as the thickness of the Py layer can not be controlled perfectly.

Figure 4.14b-d display the hysteresis curves for the three Py discs that were measured from the second batch of 50 nm Cu samples. Figure 4.14a display a hysteresis from the first batch for comparison. By inspection of the hysteresis curves, abnormalities were discovered. The abnormalities are most prominent in Figure 4.14d. When approaching saturation, the magnetization is abruptly slowed down before slowly reaching saturation magnetization. There is some uncertainty around why this effect is observed and how it has influenced other parameters such as the saturation magnetization. Contamination by some foreign magnetic material on the sample holder or defects on the samples could be possible explanations. However, it does not seem to influence the coercive field size.

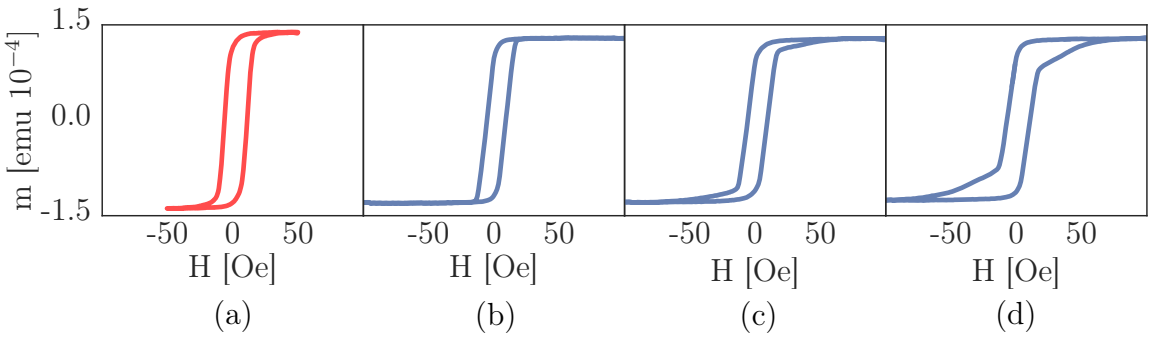

Figure 4.14: Hysteresis loops of 20 Py thin films on 50 nm Cu substrates | The data from two different batches is obtained using using VSM. **(a)** Hysteresis curve from first batch. **(b-d)** Hysteresis curves from the second batch. The measurement interval was increased to $H \in [-100, 100]$ Oe in order to reach saturation for all three samples.

Chapter 5

Conclusion

This project studies the surface properties of metal thin films and how the surface morphology influences the magnetic properties of permalloy thin films. The main aim was to provide detailed characterizations of the fabricated metal thin film surfaces and use this information to explain the dissimilarities in the magnetic properties of Py thin films deposited on the metal thin films as the morphology of the substrate changes.

Surface characteristics of Ti/Au thin films of different evaporation rates and Ti/Cu/Al thin films of different thicknesses were investigated. Deposition of Au thin films was found to be increasingly prone to spitting at increasing deposition rates, making them a poor choice for striplines. The arithmetic average and rms roughness of Ti/Cu/Al multilayer increased linearly with thickness. Replication of the deposition process yielded a 5-6 % change in the rms and arithmetic average for 50 nm Cu. Cu grain sizes were found to be in the same range as the domain wall width, making domain pinning likely occur. SEM images revealed that Py thin film growth was conformal with the film surface replicating the substrate morphology.

VSM measurements were performed at two perpendicular angles on 20 nm thick circular Py discs deposited on Ti/Cu/Al layers of different thicknesses. The behavior of the hysteresis curves was analyzed based on their shape and characteristic parameters. The findings suggest that the domain wall pinning mechanism strongly influences the size of the coercive field and that the morphology of the substrate surface is a crucial factor in the delay in domain wall motion caused by pinning. A sharper jump in the magnetization and a lower squareness determined that the effect of domain wall pinning is less prominent in samples with lower coercive fields. In general, the saturation magnetization decreased, and the coercive field size increased when the substrate rms roughness increased. However, an exception to this rule was also observed, making it hard to determine the exact behavior of the magnetic thin film based on the rms roughness alone. A lower coercive field was measured for the substrate with the lowest excess kurtosis, indicating Py films deposited on a substrate with a more bumpy-like grain structure are less affected by domain wall pinning.

5.1 Further work

Layers of Ti/Cu/Al have proven to inherit reliable surface characteristics when deposited on Si substrates, and its influence on permalloy thin films has been investigated. However, a possible solution could be etching the pattern to avoid oxidation problems and defects in the outer parts of fabricated features.

From the result presented in this thesis, we can not rule out anisotropy effects in the Py thin films on rough substrates, although it was not observed. Measurements along the full 360° circle should have been performed to investigate anisotropy effects better. Unfortunately, this requires equipment that has not been available during the work on this thesis.

One of the strong sources of motivation for this study was the possible use of metallic thin films as striplines for artificial spin ices. Typical nanomagnets in artificial spin ice structures have dimensions of 80 nm×220 nm and a thickness of 20 nm. These dimensions correspond to a length of around 4-5 times the length of the grain diameter for the Cu thin films. In this study, we have observed increased coercive field sizes, most likely due to the delay of domain wall motion caused by domain wall pinning. Delay of domain wall motion and domain wall nucleation could also affect the switching of nanomagnets. However, most of the numerical studies deal with ideal nanomagnets and neglect the presence of surface roughness. Rough surfaces will probably lead to unpredictable behavior, as we have witnessed when assessing the magnetic properties of magnetic thin films. To better understand how surface roughness influences the dynamics of artificial spin ice, an investigation of artificial spin ice structures on rough substrates could be conducted.

Bibliography

[1] G. E. Moore *et al.*, *Cramming more components onto integrated circuits*, 1965.

[2] G. E. Moore *et al.*, 'Progress in digital integrated electronics,' in *Electron devices meeting*, Washington, DC, vol. 21, 1975, pp. 11–13.

[3] I. A. Young and D. E. Nikonov, 'Principles and trends in quantum nano-electronics and nano-magnetics for beyond-cmos computing,' in *2017 47th European Solid-State Device Research Conference (ESSDERC)*, IEEE, 2017, pp. 1–5.

[4] Y. Jing, H. Luo, P. Huang and L. Qin, 'U-type piezoelectric thin-film microactuator for hard disk drives,' *IEEE Transactions on Magnetics*, vol. 41, no. 11, pp. 4309–4314, 2005. DOI: 10.1109/TMAG.2005.854235.

[5] K. Hon, Y. Kuwabiraki, M. Goto, R. Nakatani, Y. Suzuki and H. Nomura, 'Numerical simulation of artificial spin ice for reservoir computing,' *Applied Physics Express*, vol. 14, no. 3, p. 033 001, 2021.

[6] I. Gilbert, G.-W. Chern, B. Fore, Y. Lao, S. Zhang, C. Nisoli and P. Schiffer, 'Direct visualization of memory effects in artificial spin ice,' *Physical Review B*, vol. 92, no. 10, p. 104 417, 2015.

[7] F. Caravelli and C. Nisoli, 'Logical gates embedding in artificial spin ice,' *New Journal of Physics*, vol. 22, no. 10, p. 103 052, 2020.

[8] H. Arava, P. M. Derlet, J. Vijayakumar, J. Cui, N. S. Bingham, A. Kleibert and L. J. Heyderman, 'Computational logic with square rings of nanomagnets,' *Nanotechnology*, vol. 29, no. 26, p. 265 205, 2018.

[9] J. H. Jensen, E. Folven and G. Tufte, 'Computation in artificial spin ice,' in *Artificial Life Conference Proceedings*, MIT Press, 2018, pp. 15–22.

[10] R. Ravaud and G. Lemarquand, 'Comparison of the coulombian and amperian current models for calculating the magnetic field produced by radially magnetized arc-shaped permanent magnets,' *Progress In Electromagnetics Research*, vol. 95, p. 309, 2009.

[11] J. M. D. Coey, *Magnetism and Magnetic Materials*. Cambridge University Press, 2010. DOI: 10.1017/CBO9780511845000.

[12] S. Blundell, *Magnetism in condensed matter*. Oxford University Press, 2001.

[13] N. A. Spaldin, *Magnetic Materials: Fundamentals and Applications*, 2nd ed. Cambridge University Press, 2010. DOI: 10.1017/CBO9780511781599.

[14] P. Rasaili, N. K. Sharma and A. Bhattarai, 'Comparison of ferromagnetic materials: Past work, recent trends, and applications,' *Condensed Matter*, vol. 7, no. 1, p. 12, 2022.

[15] I. Rissanen *et al.*, 'Magnetization dynamics and energy dissipation in magnetic thin films,' 2019.

[16] S. Lemerle, J. Ferré, C. Chappert, V. Mathet, T. Giamarchi and P. Le Doussal, 'Domain wall creep in an ising ultrathin magnetic film,' *Physical review letters*, vol. 80, no. 4, p. 849, 1998.

[17] J. Swerts, K. Temst, N. Vandamme, C. Van Haesendonck and Y. Bruynseraede, 'Interplay between surface roughness and magnetic properties in ag/fe bilayers,' *Journal of magnetism and magnetic materials*, vol. 240, no. 1-3, pp. 380–382, 2002.

[18] L. Yin, D. Wei, N. Lei, L. Zhou, C. Tian, G. Dong, X. Jin, L. Guo, Q. Jia and R. Wu, 'Magnetocrystalline anisotropy in permalloy revisited,' *Physical review letters*, vol. 97, no. 6, p. 067 203, 2006.

[19] S. H. Skjærvø, C. H. Marrows, R. L. Stamps and L. J. Heyderman, 'Advances in artificial spin ice,' *Nature Reviews Physics*, vol. 2, no. 1, pp. 13–28, 2020.

[20] A. Farhan, P. M. Derlet, A. Kleibert, A. Balan, R. V. Chopdekar, M. Wyss, J. Perron, A. Scholl, F. Nolting and L. J. Heyderman, 'Direct observation of thermal relaxation in artificial spin ice,' *Physical review letters*, vol. 111, no. 5, p. 057 204, 2013.

[21] Z. Cui, *Nanofabrication: Principles, Capabilities and Limits*. Springer US, 2008, ISBN: 978-1-4419-4536-5.

[22] N. Sahu, B. Parija and S. Panigrahi, 'Fundamental understanding and modeling of spin coating process: A review,' *Indian Journal of Physics*, vol. 83, no. 4, pp. 493–502, 2009.

[23] O. Nalamasu, M. Cheng, A. G. Timko, V. Pol, E. Reichmanis and L. F. Thompson, 'An overview of resist processing for deep-uv lithography,' *Journal of Photopolymer Science and Technology*, vol. 4, no. 3, pp. 299–318, 1991.

[24] V. S. Smentkowski, 'Trends in sputtering,' *Progress in Surface Science*, vol. 64, no. 1-2, pp. 1–58, 2000.

[25] P. Panjan, A. Drnovšek, P. Gselman, M. Čekada and M. Panjan, 'Review of growth defects in thin films prepared by pvd techniques,' *Coatings*, vol. 10, no. 5, p. 447, 2020.

[26] M. Schütze, 'Mechanical properties of oxide scales,' *Oxidation of Metals*, vol. 44, no. 1, pp. 29–61, 1995.

[27] C. Nishimura, Y. Nagai, K. Yanagisawa and T. Toshima, 'Magnetic properties of nife films prepared using ion-beam sputtering,' *IEEE transactions on magnetics*, vol. 23, no. 5, pp. 2728–2730, 1987.

[28] M. Salou, B. Lescop, S. Rioual, A. Lebon, J. B. Youssef and B. Rouvellou, 'Initial oxidation of polycrystalline permalloy surface,' *Surface science*, vol. 602, no. 17, pp. 2901–2906, 2008.

[29] A. Khursheed, *Scanning electron microscope optics and spectrometers*. World scientific, 2011.

[30] P. Babelon, A. Dequiedt, H. Mostefa-Sba, S. Bourgeois, P. Sibillot and M. Sacilotti, 'Sem and xps studies of titanium dioxide thin films grown by mocvd,' *Thin Solid Films*, vol. 322, no. 1-2, pp. 63–67, 1998.

[31] F. J. Giessibl, 'Advances in atomic force microscopy,' *Reviews of modern physics*, vol. 75, no. 3, p. 949, 2003.

[32] D. L. Butler, 'Surface roughness measurement,' in *Encyclopedia of Microfluidics and Nanofluidics*, D. Li, Ed. Boston, MA: Springer US, 2008, pp. 1945–1949, ISBN: 978-0-387-48998-8. DOI: 10.1007/978-0-387-48998-8_1506.

[33] M. Herring, J. Mardel and B. Fox, 'The effect of material selection and manufacturing process on the surface finish of carbon fibre composites,' *Journal of Materials Processing Technology*, vol. 210, no. 6-7, pp. 926–940, 2010.

[34] J. Gerber, W. Burmester and D. J. Sellmyer, 'Simple vibrating sample magnetometer,' *Review of Scientific Instruments*, vol. 53, no. 5, pp. 691–693, 1982.

[35] D. Jordán, D. González-Chávez, D. Laura, L. L. Hilario, E. Monteblanco, A. Gutarra and L. Avilés-Félix, 'Detection of magnetic moment in thin films with a home-made vibrating sample magnetometer,' *Journal of Magnetism and Magnetic Materials*, vol. 456, pp. 56–61, 2018.

[36] S. Foner, 'The vibrating sample magnetometer: Experiences of a volunteer,' *Journal of applied physics*, vol. 79, no. 8, pp. 4740–4745, 1996.

[37] A. N. McCaughan, A. N. Tait, S. M. Buckley, D. M. Oh, J. T. Chiles, J. M. Shainline and S. W. Nam, 'Phidl: Python-based layout and geometry creation for nanolithography,' *Journal of Vacuum Science & Technology B*, vol. 39, no. 6, p. 062 601, 2021. DOI: https://doi.org/10.1116/6.0001203.

[38] micro resist technology, *MICROPOSIT™ SPR™ 700 series*, https://www.microresist.de/en/produkt/microposit-spr-700-series/.

[39] R. Strømholt, 'Simulation, design and realisation of on-chip microheaters for artificial spin ice systems,' M.S. thesis, NTNU, 2021.

[40] S. B. Kaemmer, 'Introduction to bruker's scanasyst and peakforce tapping afm technology,' 2011.

[41] D. Nečas and P. Klapetek, 'Gwyddion: An open-source software for SPM data analysis,' *Central European Journal of Physics*, vol. 10, pp. 181–188, 1 2012, ISSN: 1895-1082. DOI: 10.2478/s11534-011-0096-2.

[42] A. Khursheed and N. Karuppiah, 'A high-resolution mixed field immersion lens attachment for conventional scanning electron microscopes,' *Review of scientific instruments*, vol. 73, no. 8, pp. 2906–2909, 2002.

[43] Q. Design, *Quantum Design PPMS® VersaLab™*, https://qdusa.com/products/versalab.html.

[44] Q. Design, *Versalab User's Manual*, 8th ed. 6325 Lusk Boulevard, San Diego, CA 92121, USA: World scientific, 2015.

[45] P. Virtanen, R. Gommers, T. E. Oliphant, M. Haberland, T. Reddy, D. Cournapeau, E. Burovski, P. Peterson, W. Weckesser, J. Bright, S. J. van der Walt, M. Brett, J. Wilson, K. J. Millman, N. Mayorov, A. R. J. Nelson, E. Jones, R. Kern, E. Larson, C. J. Carey, İ. Polat, Y. Feng, E. W. Moore, J. VanderPlas, D. Laxalde, J. Perktold, R. Cimrman, I. Henriksen, E. A. Quintero, C. R. Harris, A. M. Archibald, A. H. Ribeiro, F. Pedregosa, P. van Mulbregt and SciPy 1.0 Contributors, 'SciPy 1.0: Fundamental Algorithms for Scientific Computing in Python,' *Nature Methods*, vol. 17, pp. 261–272, 2020. DOI: 10.1038/s41592-019-0686-2.

[46] A. Savitzky and M. J. Golay, 'Smoothing and differentiation of data by simplified least squares procedures.,' *Analytical chemistry*, vol. 36, no. 8, pp. 1627–1639, 1964.

[47] K. Chopra, L. Bobb and M. Francombe, 'Electrical resistivity of thin single-crystal gold films,' *Journal of Applied Physics*, vol. 34, no. 6, pp. 1699–1702, 1963.

[48] H.-G. Boyen, G. Kastle, F. Weigl, B. Koslowski, C. Dietrich, P. Ziemann, J. P. Spatz, S. Riethmuller, C. Hartmann, M. Moller *et al.*, 'Oxidation-resistant gold-55 clusters,' *Science*, vol. 297, no. 5586, pp. 1533–1536, 2002.

[49] D. Lepage, D. Carrier, A. Jiménez, J. Beauvais and J. J. Dubowski, 'Plasmonic propagations distances for interferometric surface plasmon resonance biosensing,' *Nanoscale research letters*, vol. 6, no. 1, pp. 1–7, 2011.

[50] Z. Wang and P. Wynblatt, 'The equilibrium form of pure gold crystals,' *Surface science*, vol. 398, no. 1-2, pp. 259–266, 1998.

[51] J. Heyraud and J. Metois, 'Equilibrium shape of gold crystallites on a graphite cleavage surface: Surface energies and interfacial energy,' *Acta metallurgica*, vol. 28, no. 12, pp. 1789–1797, 1980.

[52] T. Trunk, M. Redjdal, A. Kákay, M. Ruane and F. Humphrey, 'Domain wall structure in permalloy films with decreasing thickness at the bloch to néel transition,' *Journal of Applied Physics*, vol. 89, no. 11, pp. 7606–7608, 2001.

[53] F. Béron, A. Kaidatzis, M. F. Velo, L. C. Arzuza, E. M. Palmero, R. P. Del Real, D. Niarchos, K. R. Pirota and J. M. Garcıa-Martın, 'Nanometer scale hard/soft bilayer magnetic antidots,' *Nanoscale Research Letters*, vol. 11, no. 1, pp. 1–11, 2016.

[54] S. K. Vayalil, A. Koorikkat, A. K. Gopi, S. V. Roth and P. A. Kumar, 'Tailoring of uniaxial magnetic anisotropy in permalloy thin films using nanorippled si substrates,' *Journal of Physics: Condensed Matter*, vol. 32, no. 18, p. 185 804, 2020.

[55] M. Belusky, S. Lepadatu, J. Naylor and M. Vopson, 'Evidence of substrate roughness surface induced magnetic anisotropy in ni80fe20 flexible thin films,' *Journal of Magnetism and Magnetic Materials*, vol. 478, pp. 77–83, 2019.

[56] D. Allwood, G. Xiong, M. Cooke and R. Cowburn, 'Magneto-optical kerr effect analysis of magnetic nanostructures,' *Journal of Physics D: Applied Physics*, vol. 36, no. 18, p. 2175, 2003.

[57] D. Azuma, R. Hasegawa, S. Saito and M. Takahashi, 'Effect of residual strain in fe-based amorphous alloys on field induced magnetic anisotropy and domain structure,' *Journal of Applied Physics*, vol. 113, no. 17, 17A339, 2013.

[58] H. D. Young and R. A. Freedman, *Sears and Zemansky's university physics, 10th edition : test bank*. Addison-Wesley, 2000.

[59] X. Zhang, Y. Lao, J. Sklenar, N. S. Bingham, J. T. Batley, J. D. Watts, C. Nisoli, C. Leighton and P. Schiffer, 'Understanding thermal annealing of artificial spin ice,' *APL Materials*, vol. 7, no. 11, p. 111 112, 2019.

[60] A. Rohatgi, *Webplotdigitizer: Version 4.5*, 2021. [Online]. Available: `https://automeris.io/WebPlotDigitizer`.

[61] G. Zhao, L. Zhao, L. Shen, J. Zou and L. Qiu, 'Coercivity mechanisms in nanostructured permanent magnets,' *Chinese Physics B*, vol. 28, no. 7, p. 077 505, 2019.

[62] K. Chen, R. Frömter, S. Rössler, N. Mikuszeit and H. P. Oepen, 'Uniaxial magnetic anisotropy of cobalt films deposited on sputtered mgo (001) substrates,' *Physical Review B*, vol. 86, no. 6, p. 064 432, 2012.

Appendix A

Magnetization Data from Literature

The magnetization versus temperature graph for 20 nm permalloy thin films from [59] is displayed in Figure A.1. The experimental fit that was applied to obtain an estimate at room temperature is shown in Figure A.2. The curve fit was obtained using the function

$$f(T) = -a \cdot \log\left(-b/\left(T - c\right)\right), \tag{A.1}$$

where T is the temperature. a, b, and c are constants to be determined. Relevant code for the curve fit is displayed in Appendix B.

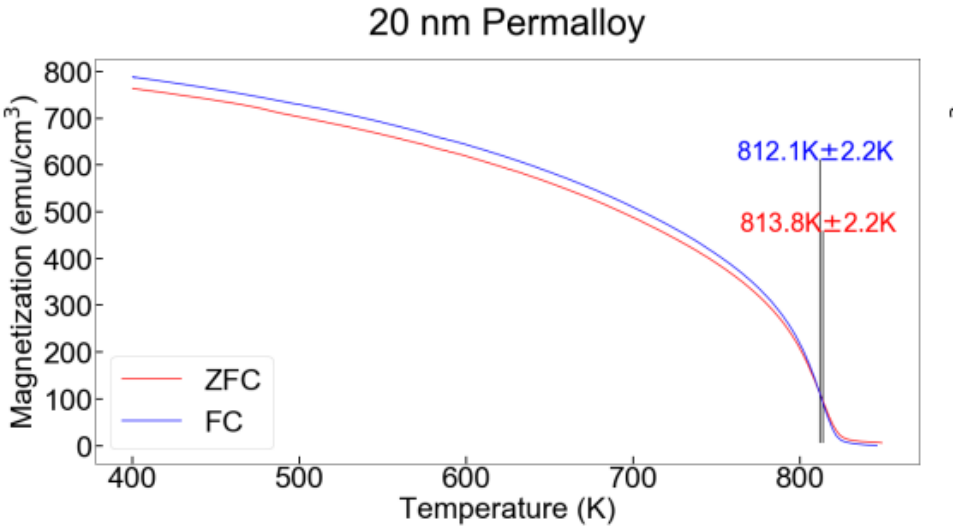

Figure A.1: Figure from [59] displaying the magnetization in 20 nm Py thin film at different temperatures.

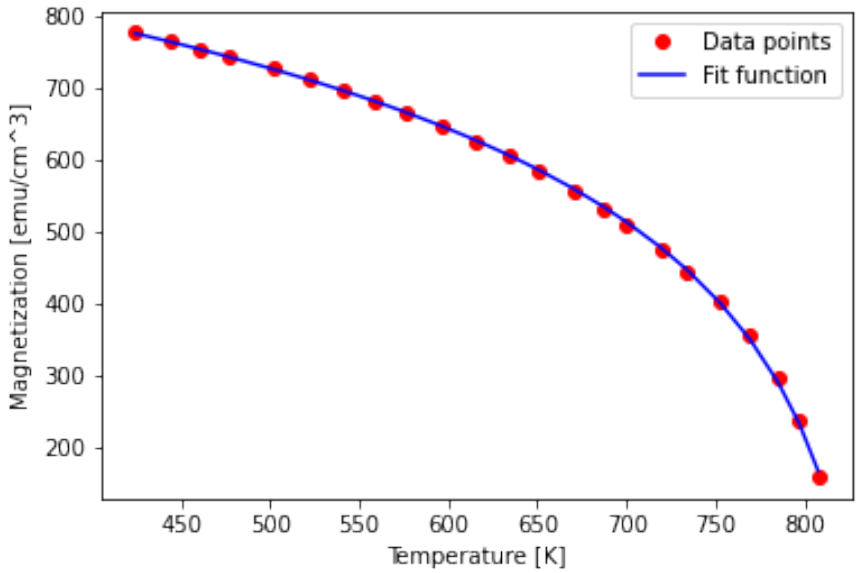

Figure A.2: Curve fit for the magnetization data. The red points are obtained from figure A.1 using webplotdigitizer. The blue curve is obtained using curve_fit from Scipy with the function $f(T) = -a \cdot \log\left(-b/\left(T - c\right)\right)$.

Appendix B

Relevant Code

Code listing B.1: The following code was used to obtain the curve fit for the magnetization data displayed in Appendix A.

```
#-----------------------------------------------------
#--------- FIT CURVE TO MAGNETIZATION DATA -----------
#-----------------------------------------------------

import numpy as np
import pandas as pd
from scipy.optimize import curve_fit

def f(x, a, b, c):
    return -a*np.log(-b/(x-c))

def getf(file):
     #Read datasheet
    df = pd.read_csv(file,
        sep=";",
        skiprows=0, engine="python")
    df.dropna()

    guess = [244, 17, 841]
    parameters, covariance = curve_fit(f, df.iloc[:,0],
                                    df.iloc[:,1], p0 = guess)
    fit_y = f(df.iloc[:,0], parameters[0],
              parameters[1], parameters[2])

    plt.plot(df.iloc[:,0], df.iloc[:,1], 'ro')
    plt.plot(df.iloc[:,0], fit_y, 'b-')
    plt.show()

    SE = np.sqrt(np.diag(covariance))
    print("Parameters:␣" + str(parameters))
    print("Standard␣error:␣" + str(SE))
    print("magnetization␣at␣300␣K:␣" + str(f(300, parameters[0],
            parameters[1], parameters[2])))

    return 0
```

Code listing B.2: Code for extracting the most important parameters and smoothing of hysteresis curves using the S-G filter.

```
#-------------------------------------------------------
#------------ Extract VSM data (function) --------------
#-------------------------------------------------------

import numpy as np
import pandas as pd
import os
from scipy.signal import savgol_filter
from scipy import asarray as ar,exp

def VSMdata(dir, windowL, **kwargs):

    title = kwargs.get('title', None)
    metalThickness = kwargs.get('thickness', str)

    os.chdir(dir)
    files = os.listdir()
    dataList = []
    dfList = pd.DataFrame(columns = ["Substrate", "Hc", "Ms", "m␣[emu/cm^3]", "m␣[A/m]"])

    # Loop through all files.
    for file in files:
        if ".dat" in file:
            sampleType = "50␣nm␣Cu␣Batch␣2" if "Batch2" in legend \
            else "50␣nm␣Cu" if "Cu␣50" in legend else "100␣nm␣Cu" \
            if "Cu␣100" in legend else "150␣nm␣Cu" if "Cu␣150" in legend else "Si"

            df = pd.read_csv(file, sep=",",
                     skiprows=30, engine="python")
            df.dropna()

            arr = df['Moment␣(emu)'].to_numpy()

            filter = savgol_filter(arr, windowL, 1)*10**4

            mSat = (np.abs(np.nanmin(filter)) + np.nanmax(filter))/(2*10**4)
            hZeroIntercepts = []

            for i in range(len(df['Moment␣(emu)'])-1):
                Mi = df['Moment␣(emu)'][i]
                Mnext = df['Moment␣(emu)'][i+1]
                Hi = df['Magnetic␣Field␣(Oe)'][i]
                Hnext = df['Magnetic␣Field␣(Oe)'][i+1]

                frac = (abs(Mi))/(abs(Mi) + abs(Mnext))
                deltaH = Hnext - Hi
                interpH = Hi + frac*deltaH
                hZeroInterceptsId = []

                if (df['Moment␣(emu)'][i] < 0 and df['Moment␣(emu)'][i+1] > 0):
                    hZeroIntercepts.append(interpH)
                    hZeroIntercepts.append(interpH)

                elif (0 < df['Moment␣(emu)'][i] and 0 > df['Moment␣(emu)'][i+1]):
                    hZeroIntercepts.append(interpH)

            Hr = (hZeroIntercepts[0] +  hZeroIntercepts[1])/2
            MrList = []
```

```
            for i in range(len(df['Magnetic Field (Oe)'])-1):
                if (df['Magnetic Field (Oe)'][i]> Hr and df['Magnetic Field (Oe)'][i+1] <= Hr):
                    MrList.append(df['Moment (emu)'][i+1])
                if (df['Magnetic Field (Oe)'][i]< Hr and df['Magnetic Field (Oe)'][i+1] >= Hr):
                    MrList.append(df['Moment (emu)'][i])

            # Append values from hysteresis
            remanentMagnetization = (MrList[0] - MrList[1])/2
            coerciveField = (hZeroIntercepts[1] - hZeroIntercepts[0])/2
            dataList.append('Msat of ' + legend + ': ' + str(mSat) + ' emu, Hc: '\
                            + str(coerciveField) + ' Oe')
            dfList = dfList.append({"Substrate": sampleType, "Hc": coerciveField, "Ms": mSat,
                    "Mr":remanentMagnetization,
                    "Mr [emu/cm^3]":remanentMagnetization/(20e-9*np.pi*1.75e-3*1.75e-3*1e6),
                    "Mr/Ms":remanentMagnetization/mSat,
                    "M [emu/cm^3]":mSat/(20e-9*np.pi*1.75e-3*1.75e-3*1e6),
                    "M [A/m]":mSat/(20e-9*np.pi*1.75e-3*1.75e-3*1e6)*1e3},
                    ignore_index = True)

    # Return either dataList or dfList
    return dfList
```

Code listing B.3: The following code was used to calculate the average vector component pointing along the mean plane, presented in subsection 4.3.3.

```
#-----------------------------------------------------------
#------- Calculate average horizontal vector length -----
#-----------------------------------------------------------

import numpy as np
import pandas as pd

def calcHorizontalVector(tanbArr, densArr):
    if len(tanbArr) != len(densArr):
        print("Fail")
        return 0
    E = 0
    norm = sum(densArr)
    for i in range(2,len(tanbArr)+2):
        E += densArr[i]*np.cos(np.arctan(tanbArr[i]))
    E = E/norm
    return E

def findMs(df):
    dfOut = pd.DataFrame()
    for i in range(len(df.columns)//2):
        name = df.columns[i*2]
        horizontalVec = calcHorizontalVector(df.iloc[:,i*2],
                df.iloc[:,i*2+1])
        dfOut[name] = [horizontalVec]
    return dfOut
```

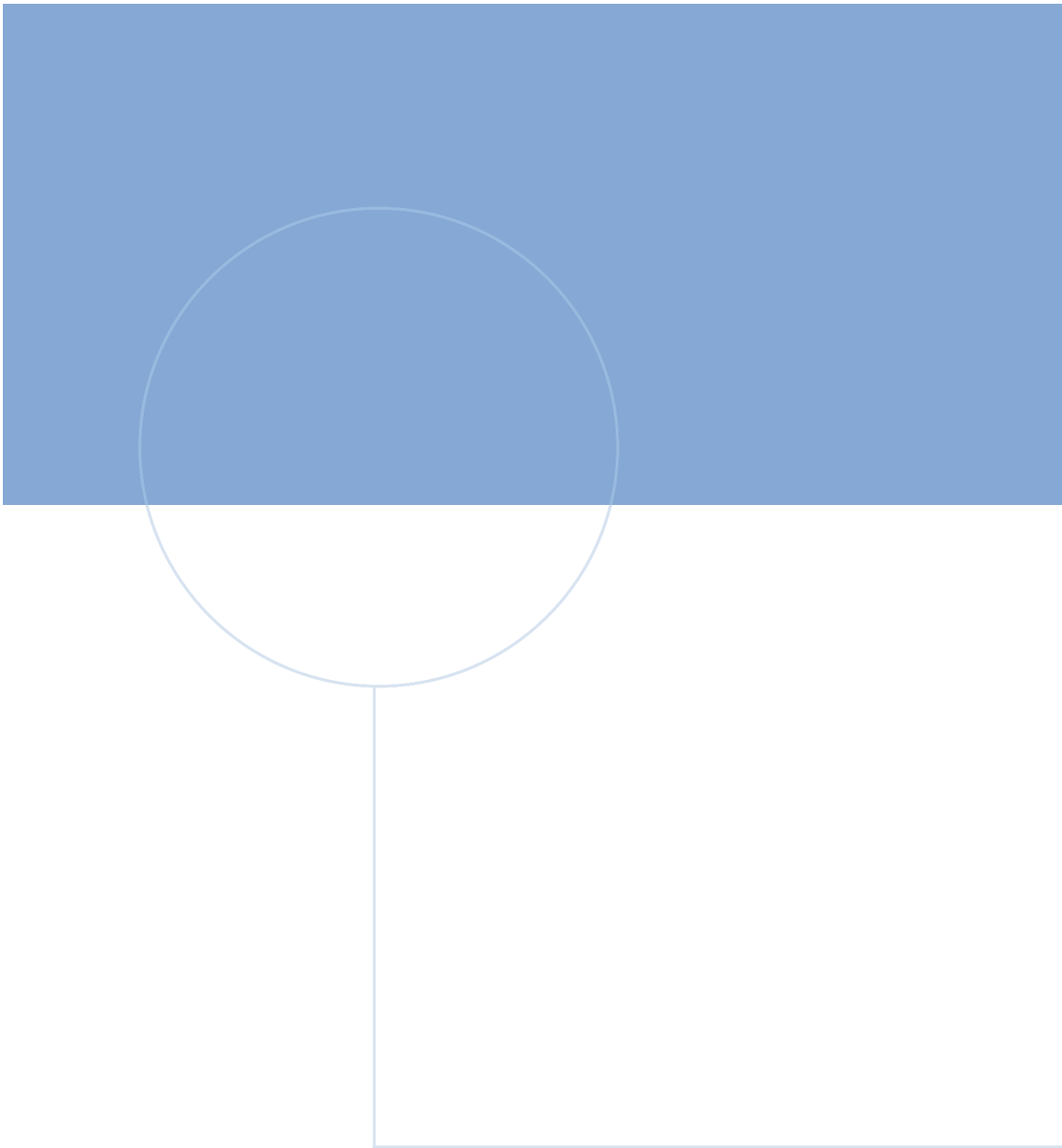

NTNU

Kunnskap for en bedre verden